

1 QBOi El Niño Southern Oscillation experiments: Assessing 2 relationships between ENSO, MJO, and QBO

3 Dillon Elsbury^{1,2}, Federico Serva³, Julie M. Caron⁴, Seung-Yoon Back⁵, Clara Orbe⁶, Jadwiga H. Richter⁴
4 James A. Anstey⁷, Neal Butchart⁸, Chih-Chieh Chen⁴, Javier García-Serrano^{9,10}, Anne Glanville⁴, Yoshio
5 Kawatani^{11,12}, Tobias Kerzenmacher¹³, Francois Lott¹⁴, Hiroaki Naoe¹⁵, Scott Osprey^{16,17}, Froila M.
6 Palmeiro^{9,18}, Seok-Woo Son⁵, Masakazu Taguchi¹⁹, Stefan Versick¹³, Shingo Watanabe²⁰, Kohei
7 Yoshida¹⁵

8
9 ¹Cooperative Institute for Research in Environmental Sciences University of Colorado Boulder, Boulder, Colorado, USA

10
11 ²NOAA/Chemical Sciences Laboratory, Boulder, Colorado, USA

12
13 ³Institute of Marine Sciences, National Research Council (ISMAR-CNR), Rome, Italy

14
15 ⁴U. S. National Science Foundation National Center for Atmospheric Research (NSF NCAR), Boulder, CO, USA

16
17 ⁵School of Earth and Environmental Sciences, Seoul National University, Seoul, South Korea

18
19 ⁶NASA Goddard Institute for Space Studies (GISS), New York, New York, USA

20
21 ⁷Canadian Centre for Climate Modelling and Analysis (CCCma), Victoria, British Columbia, Canada

22
23 ⁸Met Office Hadley Centre, Exeter, United Kingdom

24
25 ⁹Group of Meteorology, Universitat de Barcelona, Barcelona, Spain

26
27 ¹⁰Barcelona Supercomputing Center (BSC), Barcelona, Spain

28
29 ¹¹Faculty of Environmental Earth Science, Hokkaido University, Sapporo, Japan

30
31 ¹²Japan Agency for Marine-Earth Science and Technology, Yokohama, Japan

32
33 ¹³Institute of Meteorology and Climate Research-Atmospheric Trace Gases and Remote Sensing (IMK-ASF) Karlsruhe
34 Institute of Technology (KIT), Karlsruhe, Germany

35
36 ¹⁴Laboratoire de Météorologie Dynamique (LMD), Paris, France

37
38 ¹⁵Meteorological Research Institute (MRI), Tsukuba, Japan

39
40 ¹⁶National Centre for Atmospheric Science (NCAS), United Kingdom

41
42 ¹⁷Department of Physics, University of Oxford, United Kingdom

43
44 ¹⁸CMCC Foundation - Euro-Mediterranean Center on Climate Change, Italy

45
46
47
48
49
50

¹⁹ Aichi University of Education, Kariya, Japan

²⁰ Japan Agency for Marine-Earth Science and Technology (JAMSTEC), Yokohama, Japan

51 *Correspondence to:* Dillon Elsbury (delsbury@uci.edu)

52 **Abstract.** This study uses an ensemble of climate model experiments coordinated by the Quasi-Biennial Oscillation initiative
53 (QBOi) to analyze the Madden-Julian Oscillation (MJO) in the presence of either perpetual El Niño or La Niña sea surface
54 temperatures during boreal winter. In addition to the prescribed El Niño Southern Oscillation (ENSO) conditions, the nine
55 models internally generate QBOs, meaning each may influence the MJO. Objectives of our analyses are to assess the response
56 of the MJO to strong idealized ENSO forcing and look for evidence of a QBO influence on the MJO in a multi-model context.
57 The diagnostics used include wavenumber-frequency spectra of tropical convective and dynamical fields, measures of MJO
58 lifetime, an evaluation of MJO diversity and visualization of MJO vertical structure, as well as an assessment of QBO
59 morphology and the QBO’s impact on tropical convection. Kelvin wave spectral power increases in the El Niño simulations
60 whereas equatorial Rossby waves power is stronger in the La Niña simulations. All models simulate faster MJO propagation
61 under El Niño conditions. This change in speed is corroborated by the MJO diversity analysis, which reveals that models better
62 reproduce the observed “fast propagating” and “standing” MJO archetypes given perpetual El Niño and La Niña, respectively.
63 Regardless of ENSO, QBO descent into the lower stratosphere is underestimated and we detect little QBO influence on tropical
64 tropopause stability and MJO activity. With little influence from the QBO on the MJO activity in these runs, we can be
65 confident that the aforementioned changes in the MJO indeed arise from the different ENSO boundary conditions.

66 **1 Introduction**

67 The tropical circulation is influenced by various forms of internal variability, each operating at different timescales, yet still
68 influencing each other. The Madden-Julian Oscillation (MJO) is dominant at intraseasonal timescales (Madden and Julian
69 1994; Lin, 2022). It consists of large-scale eastward propagating fluctuations in tropical precipitation and circulation that
70 traverse the Indian Ocean and Maritime Continent through to the Pacific over roughly 30 to 60 days (Hendon and Salby 1994).
71 MJO variability fluctuates a lot year to year as does other variability in the climate system.

72
73 At interannual timescales, the El Niño Southern Oscillation (ENSO; Philander, 1990) is one of the most consequential sources
74 of tropical tropospheric variability. It is characterized by shifting patterns of sea surface temperatures (SSTs) and associated
75 changes in ocean and atmospheric circulations in the tropical Pacific. ENSO varies on timescales between two to seven years,
76 and consists of three phases, the warm El Niño, the cold La Niña and a “neutral” phase where neither polarity dominates. Also
77 operating at interannual timescales is the Quasi Biennial Oscillation (QBO), which is the dominant mode of variability in the
78 lower tropical stratosphere, defined by alternating easterly and westerly shear zones descending from 5 to 100 hPa with an

79 average periodicity of 28 months (Baldwin et al. 2001).

80

81 The MJO, ENSO, and QBO are known to influence each other in various ways. ENSO's La Niña and El Niño phases are
82 associated with shifts of intraseasonal tropical atmospheric variability like the MJO towards the Indo-Pacific Warm Pool and
83 Date Line, respectively (Kessler 2001; Tam and Lau 2005). In addition, ENSO can influence the amount of time the MJO
84 spends in particular Wheeler and Hendon (2004) MJO phases and the duration of MJO events overall, which are shorter during
85 El Niño and longer during La Niña (Pohl and Matthews 2007; Pang et al. 2016; Wei and Ren 2019; Wang et al. 2019; Dasgupta
86 et al. 2021; Fernandes and Grimm 2023).

87

88 Nonetheless, not all research finds strong links between ENSO and seasonal-mean MJO activity. Slingo et al. (1999) found
89 that the observed intraseasonally filtered zonal mean 200 hPa zonal wind (their metric of "MJO activity") is weakly dependent
90 on ENSO phase. They affirmed this further by using an ensemble of AMIP simulations. Hendon et al. (1999) validated and
91 refined their definition of MJO activity, finding it to capture the salient features of the MJO and again that its variability is
92 mostly independent of ENSO. These results also align with those of Newman et al. (2009) who showed that air-sea coupling
93 has a small effect on intraseasonal atmospheric variability in empirical models that run with and without atmosphere-ocean
94 interaction. With these results in mind, it is less clear how the MJO should respond to the ENSO conditions prescribed in our
95 simulations. In fact, a common idea amongst the studies just mentioned is that the MJO's interannual variability originates
96 predominantly from internal atmospheric processes other than those associated with ENSO.

97

98 It is increasingly recognized that the easterly and westerly phases of the QBO exert an influence on the MJO (Yoo and Son,
99 2016; Son et al. 2017; Sakaeda et al. 2020; Martin et al. 2021; Jin et al. 2023; Huang et al. 2023). The MJO's amplitude is
100 stronger during easterly QBO boreal winters compared to westerly QBO winters over the observed record since 1979 (Yoo
101 and Son 2016; Densmore et al. 2019). However, despite improvement in the representation of simulated QBOs (Richter et al.
102 2020) and MJOs (Ahn et al. 2020) across model generations, current free-running Earth system models generally do not
103 simulate the QBO-MJO relationship (Kim et al. 2020; Lim and Son 2020; Martin et al. 2023), nor do they simulate a
104 sufficiently strong tropical tropopause response to the QBO (Serva et al. 2022). Further complicating interpretation is a
105 tendency for easterly QBO boreal winters to co-occur with La Niña events, introducing ambiguity about the source of MJO
106 modulation (Randall et al. 2023).

107

108 In this study, we document the influence of ENSO on the MJO using a multi-model ensemble of idealized experiments with
109 perpetual El Niño and La Niña forcings. These simulations were coordinated by the Atmospheric Processes And their Role in
110 Climate (APARC, previously "SPARC") Quasi-Biennial Oscillation initiative (QBOi, Butchart et al. 2018). In addition to
111 prescribing ENSO, the models internally generate QBOs, meaning both types of interannual internal variability may modulate
112 the MJO in these experiments. Our aim is to assess the extent to which model behavior is consistent with previously reported
113 ENSO-MJO relationships, recognizing that past studies have found different ENSO-MJO links and that the simulated QBOs

114 may also project onto the MJOs. The coordinated QBOi protocol allows us to revisit these relationship in a controlled
115 framework that isolates atmospheric responses to fixed, high-amplitude ENSO SSTs across many models. These perpetual
116 ENSO conditions represent the strongest observed El Niños and La Niñas and offer an upper bound on ENSO’s effect on MJO
117 characteristics, providing a high signal-to-noise database for studying this connection. We also selectively incorporate Phase
118 1 QBOi experiments, performed as 1979-2009 Atmospheric Model Intercomparison Project experiments, and hence, more
119 representative of typical ENSO amplitudes (Butchart et al. 2018, Experiment 1). Unlike Coupled or Atmospheric Model
120 Intercomparison Project experiments, or historical reanalysis datasets, these simulations avoid complications associated with
121 time-evolving forcings, event-to-event ENSO variability, and background SST biases. On the other hand, while perpetual
122 ENSO conditions help isolate atmospheric responses, they also preclude direct comparison with observation-based datasets,
123 which include event-to-event variability, for example. The perpetual-ENSO experiments used here are a continuation of the
124 QBOi Phase 1 experiments and have companion studies that examine ENSO’s effect on the QBO (Kawatani et al., 2025) and
125 the combined influence of ENSO and the QBO on global teleconnections (Naoe et al., 2025).

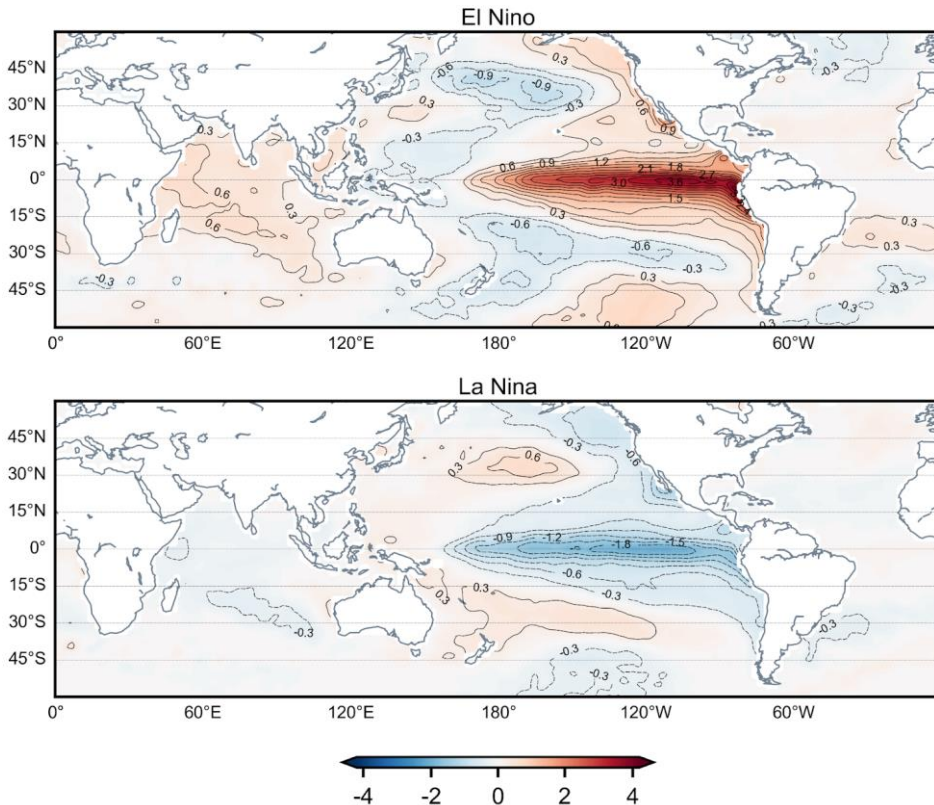
126 **2 Methods**

127 **2.1 Experimental setup**

128 Butchart et al. (2018) established a set of simplified modeling experiments for Phase 1 of the QBOi. Their Experiment 2, the
129 “present-day time slice” simulation, forms the basis for these perpetual ENSO simulations. It was designed to allow for an
130 evaluation of the accuracy of modeled QBOs under present-day conditions, that is, how the model QBOs operate in a climate
131 forced with fixed repeating annual cycles of global sea surface temperature (SSTs), sea ice concentration (SIC), and external
132 forcings representative of the time averaged 1988-2007 state.

133
134 The perpetual ENSO runs analyzed here are equivalent to Experiment 2, but with global El Niño or La Niña SST anomalies
135 superimposed on top of the climatological SST forcing. An assessment of the MJO is not conducted for Experiment 2 because
136 essential variables such as daily horizontal winds, outgoing longwave radiation (OLR), and precipitation, were not archived.
137 In creating the composite El Niño or La Niña forcings, the characterization of ENSO follows the Japan Meteorological Agency
138 (JMA) convention, where ENSO is defined by the spatially averaged NINO.3 (5°S-5°N, 150°W-90°W) monthly SST anomalies
139 from 1950-2016. Anomalies are defined as deviations from the climatological seasonal cycle and computed relative to the
140 most recent sliding 30-year period of JMA COBE-SST version 1 data (JMA, 2006). The anomalies are smoothed using a five-
141 month running mean and the periods during which the anomalies exceed 0.5°C (-0.5°C) for at least six consecutive months
142 are labeled as El Niño (La Niña) periods. However, after averaging the SST anomalies for all El Niño Januarys, Februarys,
143 etc., and doing the same for La Niña, the composite average annual cycles of El Niño and La Niña SSTs show only modest
144 amplitudes (e.g., 1.92 °C for El Niño Januarys). To amplify the atmospheric response to ENSO in the simulations and increase
145 the signal-to-noise ratio, the annual cycles are multiplied by 1.8 and 1.4, respectively, making their amplitudes comparable to
146 the strongest observed ENSO events. A similar scaling is applied to the corresponding global signatures in NINO.3 SST
147 anomalies (Fig. 1), which are superimposed on 1988–2007 climatological SSTs and prescribed in the models. Note that this

148 procedure does not completely capture the development, mature phase, and decay of all observed El Niño events, due to
 149 diversity in the evolutions of events. We refer the reader to Kawatani et al. (2025) for more details on the experimental design
 150 and sensitivity of the model QBOs.



151
 152 **Figure 1: November-April composites of the El Niño (top) and La Niña (bottom) JMA COBE SST anomalies (units K) that are**
 153 **prescribed in the perpetual ENSO simulations.**

154 In addition to the prominent El Niño and La Niña signals, the November-April (NDJFMA) SSTs shown in Figure 1 include
 155 the signatures of the basin-scale Interdecadal Pacific Oscillation (IPO) (Henley et al. 2015) and Indian Ocean SSTs that are in
 156 phase with ENSO. In some regions like the tropical Pacific and Indian Oceans, the amplitude of the global SSTs associated
 157 with the El Niño are roughly double that of La Niña (Fig. 1).

158
 159 **2.2 Models**

160
 161 *Table 1: The models used in this study, the horizontal (given as spectral triangular truncation, T , or longitude-latitude increments) and*
 162 *vertical configuration (number of levels and model top, in hPa), the number of years per simulation, and relevant literature for the convective*
 163 *schemes. Only one realization is used from each model.*

Model	Horizontal resolution	Vertical levels (top, hPa)	Number of years	Convective parameterizations
EC-EARTH3.3	T255	91 (0.01)	101	Bechtold (2014)
ECHAM5sh	T63	95 (0.01)	40	Tiedtke (1989), Nordeng (1994)
EMAC	T42	90(0.01)	106	Tiedtke (1989)
LMDz6	2°-1.25°	79 (0.015)	80	Emanuel (1991), Hourdin et al. (2013)
GISS-E2-2-G	2°-2.5°	102 (0.002)	30	Rind et al. (2020); Kelley et al. (2020)
MIROC-AGCM-LL	T106	72 (1.2)	100	Pan and Randall (1998); Emori et al. (2001)
MIROC-ESM	T42	80 (0.0036)	100	Pan and Randall (1998); Emori et al. (2001)
MRI-ESM2.0	T159	80 (0.01)	50	Yukimoto et al. (2019)
CESM1(WACCM5-110L)	1.25°-0.94°	110 (6.1E-6)	101	Zhang and McFarlane (1995)

164

165 The models considered are listed in Table 1 along with the number of years analyzed for each model and references on each
166 model's convective parameterization. These parameterizations impact the representation of tropical phenomena (Holt et al.
167 2020; Kawatani et al., 2025), including the simulation of intraseasonal oscillations (Ham and Hong, 2013). For example, past
168 sensitivity tests with the version of MIROC-ESM that we use here have shown that its cumulus parameterization struggles to
169 simulate an MJO of realistic amplitude with capability to propagate over the Maritime Continent (Miura et al. 2012). The
170 updated scheme (Chikira and Sugiyama 2010) in use in newer versions of the model, MIROC6, has helped ameliorate these
171 issues (Ahn et al. 2017; 2020). The importance of simulated convection-circulation coupling has been identified for other
172 models (Kim et al. 2014; Zhu et al. 2020; Wang et al. 2022).

173 **2.3 Observation-based reference data**

174 To be consistent with previous studies (e.g., Wei and Ren 2019), the ENSO-MJO relationship is considered during
175 November-April. The six historical La Niña years, where the year is associated with November, are 1970, 1984, 1988, 2017,
176 2020, and 2021 and the eight El Niño years are 1968, 1982, 1986, 1991, 1997, 2009, 2015, 2018. Each corresponds to an
177 instance when the smoothed Niño3 anomalies exceed $\pm 0.5^\circ\text{C}$ for at least six consecutive months. For comparison with the
178 models, the subsequent analyses include “observed” El Niño and La Niña composites, formed by averaged deseasonalized
179 1959-2022 ERA5 reanalysis (Hersbach et al. 2020) over the years. Unlike the model simulations, which prescribe ENSO
180 SST anomalies scaled by factors of 1.8 (El Niño) and 1.4 (La Niña), the ERA5 composites reflect unscaled, event-based
181 variability. While this distinction makes direct comparison between models and reanalysis imperfect, ERA5 nonetheless
182 provides a useful benchmark for expected atmospheric responses. The ERA5 El Niño and La Niña composites are best
183 interpreted in relation to each other, rather than as strict analogs to the simulations.

184 Satellite-based daily precipitation estimates from a 1996-2023 Global Precipitation Climatology Project (GPCP, v1.3) record
185 (Huffman et al. 2001; Adler et al. 2017) are used to assess ENSO-related precipitation anomalies, as is NOAA Interpolated
186 Outgoing Longwave Radiation (Liebmann and Smith 1996). For these analyses, El Niño and La Niña years are defined as
187 ± 1 variations in standardized November-April Niño3 anomalies, yielding 1997, 2009, and 2015, and La Niña years as
188 1999, 2007, and 2010. Unlike ERA5, where cloud fields and precipitation are parameterized without direct assimilation,
189 satellite-based datasets provide a more direct observational reference, particularly valuable in the tropics where reanalysis
190 precipitation is known to be less reliable (Gehne et al. 2016).

191 **2.4 MJO analyses**

192 We implement a number of widely-used methods to evaluate the MJO in the perpetual ENSO simulations. In the interest of
193 exploring changes to MJO lifetime by ENSO phase as well as visualizing the MJO’s vertical structure, we compute Real-time
194 Multivariate MJO indices (RMMs) for each perpetual ENSO simulation using the same methodology as Wheeler and Hendon
195 (2004, WH04). The RMMs are derived from a combined empirical orthogonal function (EOF) analysis of tropically averaged
196 (15°S - 15°N) anomalous daily outgoing longwave radiation (OLR), 200-hPa zonal wind (U200), and 850-hPa zonal wind
197 (U850). As in WH04, we deseasonalize, remove interannual variability, and normalize the anomalies by their global variance.
198 To enable a fairer comparison between the models and reanalysis, we project the anomalous model fields onto the 1959-2022
199 ERA5 WH04 EOFs; projecting onto each model’s respective ENSO simulation instead does not change the conclusions. Daily
200 OLR and U200 were not available for two models (GISS-E2-2-G and LMDz6) so their RMMs are computed using U250 and
201 U850.

202
203 The number of MJO events within a given data set is tallied like in Pohl and Matthews (2007) by counting the number of times
204 the MJO makes a complete rotation through its RMM1 and RMM2 phase space. Average lifetime and MJO amplitudes

205 $(\sqrt{(RMM1^2) + (RMM2^2)})$ are computed across events. To visualize the MJO’s vertical structure, latitudinally averaged
206 10°S-10°N longitude-pressure cross-section of zonal wind and temperature are projected onto the RMMs using the same steps
207 as Hendon and Abhik (2018), but applied across ENSO years in the present study rather than QBO years.

208

209 The MJO is visualized using two related wavenumber–frequency approaches. Both Fourier transform deseasonalized and
210 detrended, highpass filtered, tapered time-longitude data, reorder coefficients into eastward/westward components, and
211 compute power spectra to isolate intraseasonal variability. The CLIVAR/MJO metric (Waliser et al. 2009) applies this to
212 centered November-April segments of tropical U850, yielding single variable power for eastward and westward disturbances
213 (Figure 3). The Wheeler and Kiladis (1999) style analysis is similar, but designed to diagnose the broader family of
214 convectively coupled equatorial waves alongside the MJO: we linearly detrend multiyear daily fields, highpass filter at 96 days,
215 use overlapping 96-day segments (65-day overlap), perform successive longitude–time transforms, recover symmetric and
216 antisymmetric spectra about the equator, and normalize by a smoothed background; results are presented as the ratio of raw
217 symmetric daily mean precipitation power to background (Figure 2). To sharpen the MJO and facilitate comparison with the
218 CLIVAR metric, our Wheeler-Kiladis implementation also subsets data to November-April. For model evaluation, spectra are
219 divided by each model’s perpetual ENSO background, whereas GCPP (ERA5) El Niño and La Niña spectra are compared to
220 a common 1996-2022 (1959–2022) background; GPCP and ERA5 conclusions are insensitive to using regime specific
221 backgrounds.

222

223 We also implement an MJO diversity analysis in which MJO events are classified into distinct types based on their propagation
224 characteristics using k-means clustering (Wang et al. 2019). Each MJO event is binned as one of four archetypes, “standing”
225 or “jumping” MJOs, which propagate across the Indian Ocean, but are distinguished by reemergence of the MJO over the
226 western Pacific during jumping events, and “slow” or “fast” MJOs, which both continuously propagate across the Maritime
227 Continent, but at different speeds. An MJO event occurs when the 20-70 day bandpass-filtered OLR anomalies (from seasonal
228 cycle) averaged over the equatorial Indian Ocean (10°S-10°N, 75°E-95°E) are smaller than negative one standard deviation
229 for five successive days; the reference day (day 0) is the day of minimum OLR. The MJO events are categorized by a k-means
230 clustering of the enhanced convective signal (OLR anomalies under -5 Wm^{-2}) of the latitudinally averaged 10°S to 10°N time-
231 longitude OLR anomalies taken over 60°E to 180°E and over a 31-day period from day -10 to day 20. For brevity, we omit
232 further diversity analysis methodological details, for which we refer the reader to Back et al. (2024) for all steps. Unlike Wang
233 et al. (2019), in which initial centroids for clustering are randomly chosen, initial centroids for model MJO events are set to
234 those of the four observation-based clusters, allowing the present study to evaluate how well climate models reproduce
235 observed MJO diversity with minimal subjectivity.

236 2.5 QBO and analyses

237 The space-time form of the QBOs varies from model to model as each is generated with different amounts of forcing from
238 resolved waves and parameterized non-orographic gravity wave drag. Properties of these models that are particularly relevant
239 for simulating the QBOs are listed in Butchart et al. (2018), details on QBO morphology (e.g., its amplitude, latitudinal width)
240 given the observed SST record are presented in Bushell et al. (2022), and the relative contribution of resolved and
241 parameterized tropical waves to forcing the QBO is analyzed in detail in Holt et al. (2020). Of note, MIROC-AGCM-LL's
242 QBO is forced solely by resolved waves. As EC-EARTH and GISS-E2-2-G did not contribute to some of the earliest QBO
243 analyses, relevant details on their internal QBOs can be found in Serva et al. (2024) and Rind et al. (2014, 2020), respectively.
244 For a thorough analysis of how the QBO responds to the perpetual ENSO simulations, we refer the reader to Kawatani et al.
245 (2025).

246
247 To help clarify the ability of the QBOs to interact with the MJOs, we use established metrics to characterize the morphology
248 of the ERA5 and model QBOs. The main field used to document QBO morphology is the monthly zonal-mean zonal wind.
249 "QBO cycles" (consecutive easterly/westerly phases) are identified by marking the first month when the deseasonalized and
250 smoothed (5-month running mean) 20 hPa 5°S-5°N wind changes from westerly to easterly, ending one month before the next
251 transition at 20 hPa (Kawatani et al. 2019). From these cycles, we calculate average QBO easterly, westerly, and total
252 amplitudes using the QBO "transition time" methodology of Richter et al. (2020). The easterly (westerly) amplitude is equal
253 to the average of the minimum (maximum) monthly QBO winds from each QBO cycle. The QBO cycles are used further to
254 calculate minimum, mean, and maximum QBO periodicity statistics. These statistics are a key result of Kawatani et al. (2025)
255 and are discussed thoroughly there. In short, the periodicity of the QBO decreases in all El Niño simulations and increases in
256 all La Niña simulations, which is attributed to ENSO modulating convection and the low-frequency circulation, thereby
257 influencing generation of tropical waves and their filtering by the large-scale circulation and the QBO. For the purposes of the
258 present study, the minimum and maximum periodicities are required to evaluate the QBO's spatial structure, defined as the
259 latitude-pressure cross sections of each data set's QBO Fourier amplitude. These are made by applying a discrete Fourier
260 transform in time to the multi-year monthly zonal-mean zonal wind at each pressure-latitude grid point and dividing the sum
261 of squares of the amplitudes of the harmonics corresponding to periods between the minimum and maximum QBO periods by
262 the sum of squares of the amplitudes of all harmonics. This ratio is subsequently multiplied by the standard deviation of the
263 zonal-mean zonal wind (Pascoe et al. 2005). Using this QBO Fourier amplitude, the lowest altitude the QBO reaches, its
264 vertical extent (i.e., how tall it is), and its latitudinal extent are defined as in Schenzinger et al. (2017), except that here the
265 QBO's maximum amplitude is assumed to be at 20 hPa for all models and ERA5.

266
267 QBO impact on the MJO is assessed using the techniques of Klotzbach et al. (2019) and Kim et al. (2020). Following the prior,
268 we make scatterplots of December-February warm-pool (10°S-10°N, 45°E-180°E) averaged tropopause stability (100 hPa
269 minus 200 hPa temperature) versus December-February MJO amplitude as a function of QBO phase (sign of DJF averaged
270 5°S-5°N 50 hPa zonal mean zonal-wind) for each of the simulations. MJO amplitude is expected to increase as tropopause

271 stability decreases, which happens during the easterly QBO phase. As in Kim et al. (2020), MJO activity is also computed as
272 a function of QBO phase. Specifically, MJO-filtered OLR is calculated following Wheeler and Kiladis (1999) with one
273 exception, the full time series is detrended rather than using 96-day overlapping segments. To minimize spectral leakage, 5%
274 of the data are tapered to zero at the ends of the timeseries. After tapering, a complex Fourier Transform is performed, and the
275 spectral wavenumber-frequency data are filtered to retain only the eastward propagating coefficients for 20-100 day periods
276 and wavenumbers 1-5. MJO activity is then defined as the standard deviation of the MJO-filtered OLR across all December-
277 February days that fall into a particular category, for instance all years, easterly QBO years or westerly QBO years. For this
278 analysis, easterly and westerly QBO years are defined as those which exceed +/- 0.5 standard deviation of the 50 hPa monthly
279 zonal wind anomalies, seasonally smoothed and averaged over 10°S to 10°N. We allow the QBO to be defined differently
280 between the Klotzbach and Kim et al. Analyses; here we prioritize using the aforementioned metrics in their original form
281 rather than using customizing them.

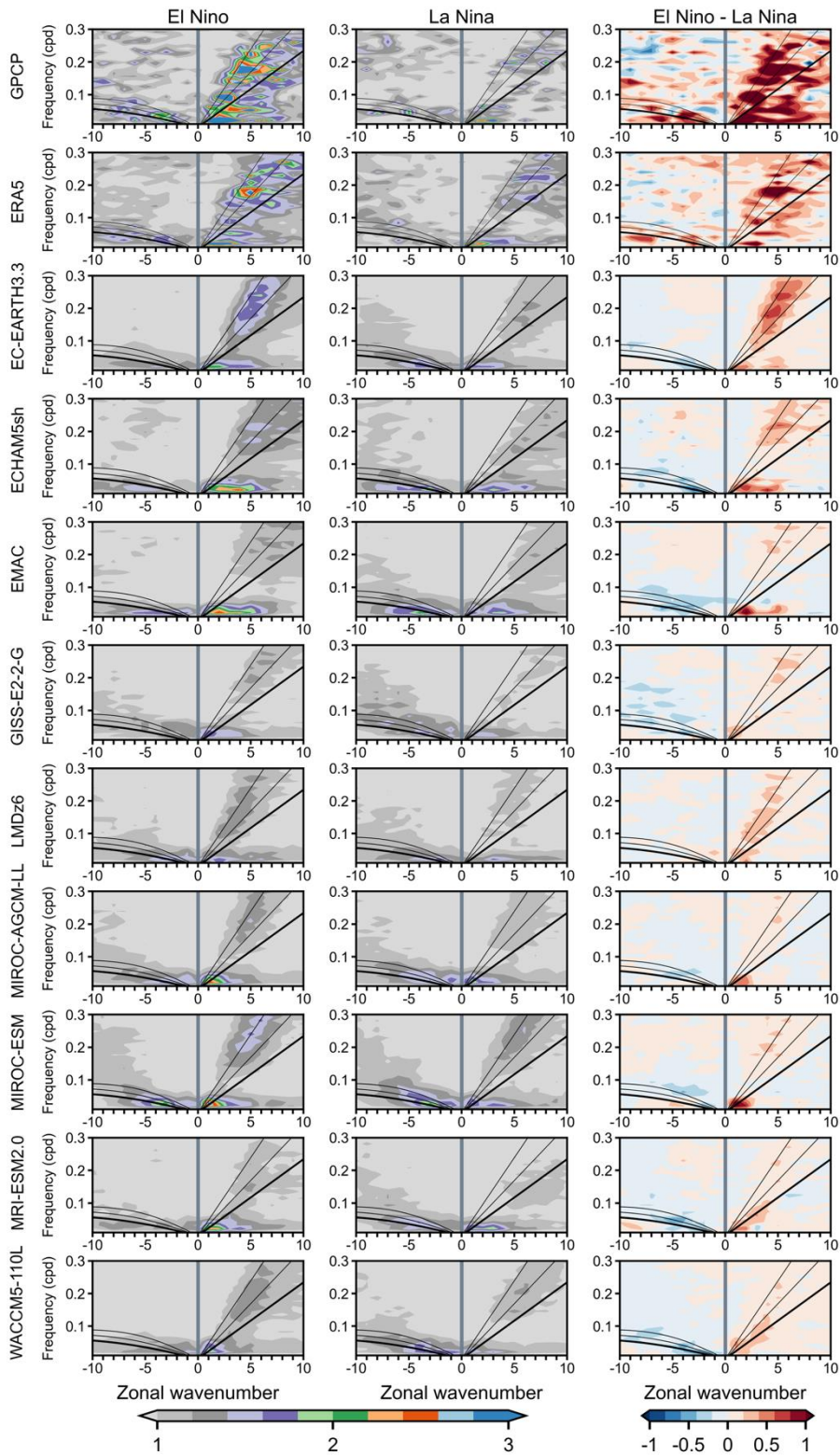
282 **3 Results**

283 **3.1 ENSO-MJO interaction**

284 Before examining the influence of ENSO on MJO, we evaluate some of the other large-scale tropical phenomena that the
285 models simulate. Convectively coupled waves are relevant because they comprise the space-time structure of the MJO and can
286 influence its propagation by modulating the tropical circulation and the distribution of moisture that the MJO encounters
287 (Kiladis et al. 2009; Wang et al. 2019; Wei and Ren 2019; Berrington et al. 2022; Wang and Li 2022). Aspects of the waves,
288 such as their phase speed, vary depending on the low frequency circulation (Roundy 2012). Hence, the amplification of the
289 Walker Circulation by La Niña and the weakening of it by El Niño (Fig. S1) provide a pathway for the perpetual ENSO
290 forcings to modulate the waves and perhaps the MJO. Applying similar methods to Wheeler and Kiladis (1999), we visualize
291 the waves by computing the spectral power of ERA5 and model daily-averaged precipitation as a function of wavenumber and
292 frequency. Figure 2 shows the precipitation spectra for phenomena symmetric about the equator, taken over November-April
293 and 15°S-15°N. Three dispersion curves, as in Matsuno (1966), corresponding to equivalent depths of 10, 25, and 50 meters
294 are also superimposed; these curves are derived using the dispersion relations for equatorially trapped waves and they are co-
295 located with modes of organized convection, with larger equivalent depths corresponding to faster phase speeds.

296
297 The GPCP panels in row one draw on only three La Niña and three El Niño years, while the ERA5 panels in row two use just
298 six La Niña and eight El Niño years, resulting in signals that are noisier than the models' multi-decade averages. Power is
299 typically the highest amplitude in GPCP, then ERA5, and weakest in the models. Spectral signals associated with the eastward
300 propagating Kelvin wave move up and to the right on each panel, spanning sub-planetary low frequency ($\sim k = 3, 25$ days)
301 scales to synoptic ($k = 4+$) sub-weekly scales. Relative to GPCP and ERA5, the models underestimate the strength of the
302 Kelvin wave irrespective of the type of ENSO forcing, but have worse difficulties in the El Niño simulation. Power associated
303 with the westward propagating equatorial Rossby wave is evident on the left side of each panel between wavenumbers 1-10

304 and timescales of 10 days to five weeks. Overall, the models do a reasonable job of simulating the spectral amplitude of
305 equatorial Rossby waves, although it is too strong for some models (EMAC, MIROC-ESM), especially in their La Niña
306 simulations (Fig. S2).
307



309 **Figure 2: Wavenumber-frequency spectrum of the symmetric component of 15°S-15°N November-April precipitation plotted as the**
310 **ratio between raw symmetric precipitation and a smoothed red noise background spectrum. The eastward (right) side of the**
311 **spectrum includes three Kelvin wave dispersion curves in black, of which the thickest curve corresponds to the equivalent depth of**
312 **12 meters, and the others to 25 and 50 meters, respectively. Similar dispersion curve plotting conventions are used on the westward**
313 **(left) side of the spectrum where the curves overlay the equatorial Rossby wave power. Column one corresponds to El Niño, column**
314 **two to La Niña, and column three to their difference, which is computed as (El Niño symmetric minus El Niño background) minus**
315 **(La Niña symmetric minus La Niña background). Computing the third column as (El Niño symmetric) minus (La Niña symmetric)**
316 **yields similar conclusions (not shown).**
317

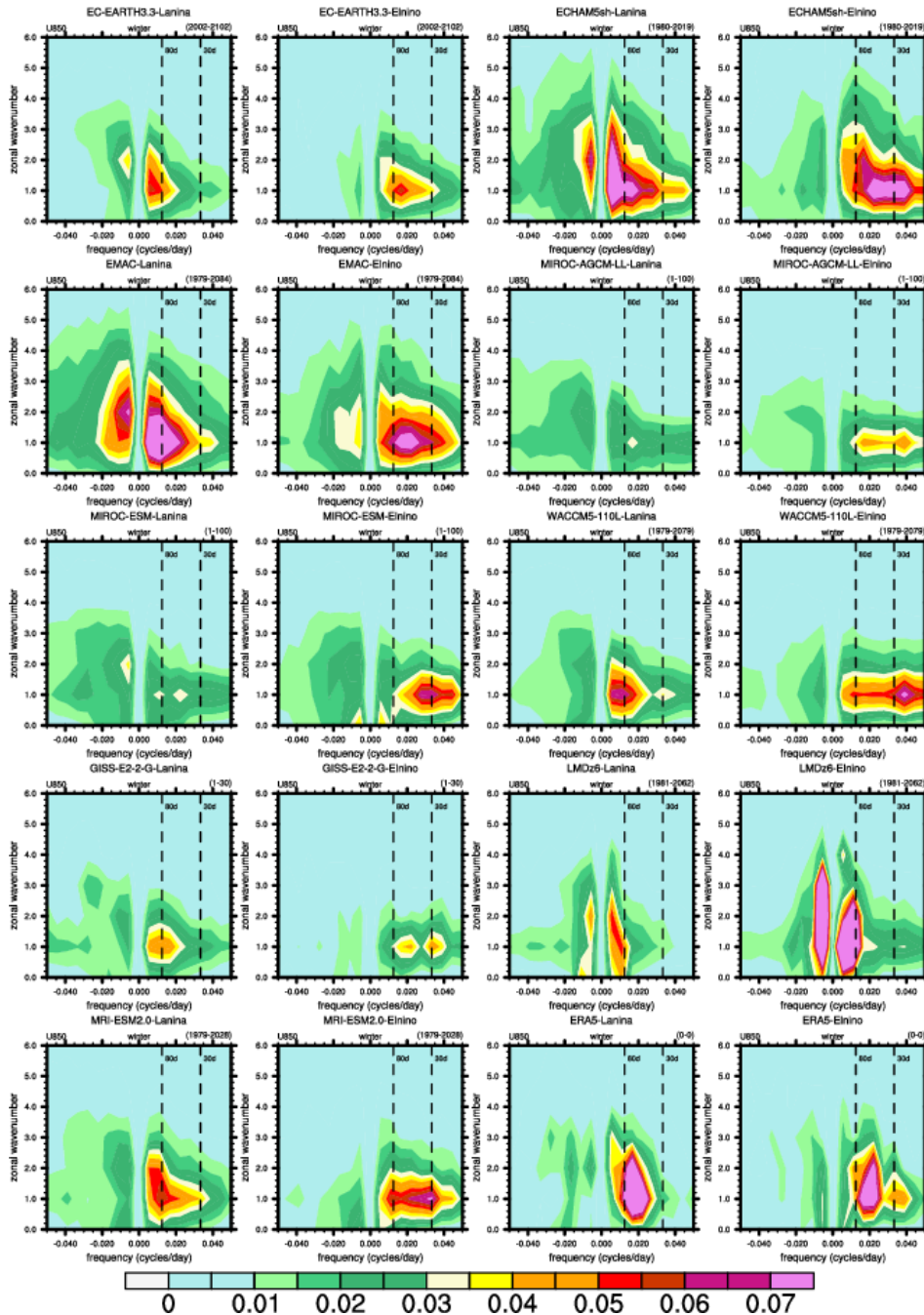
318 The effect of ENSO phase on each wave is revealed by the rightmost column of Figure 2, which shows El Niño (column one)
319 minus La Niña (column two) differences, where red means stronger power during El Niño and blue means larger power during
320 La Niña. All models simulate stronger Kelvin waves in their El Niño simulation, particularly along the deeper equivalent depth
321 ($n = 25, 50$ meters) dispersion curves. This implies faster Kelvin wave phase speeds during El Niño. Examining the El Niño
322 column, the alignment of the Kelvin wave power along these particular curves is demonstrated by EC-EARTH3.3, GISS-E2-
323 2-G, LMDz6, MIROC-AGCM-LL, MIROC-ESM, MRI-ESM2.0 and (CESM1) WACCM5-110L, hereafter just “WACCM5-
324 110L.” The remaining models, ECHAM5sh and EMAC (both ECHAM-based models), differ in that their El Niño Kelvin wave
325 power is weighted towards higher zonal wavenumbers for frequencies below 0.2 cpd. Similar to the models, GPCP and ERA5
326 shows large sporadic increases in Kelvin wave power along deeper equivalent depth dispersion curves during El Niño
327 compared to La Niña. In contrast, for the westward propagating equatorial Rossby wave, GPCP and ERA5 indicate stronger
328 power during El Niño, whereas all models simulate stronger Rossby wave power during La Niña. This discontinuity arises
329 from models underestimating average equatorial Rossby wave spectral power during El Niño, while overestimating power
330 during La Niña relative to GPCP and ERA5 (Fig. S2).

331
332 Having found changes in the convectively coupled waves due to ENSO, perhaps the model MJOs also behave differently given
333 ENSO state. Broadly speaking, Figure 2 shows that the models include MJOs as indicated by the maxima in spectral power at
334 intraseasonal timescales ($\ll 0.1$ cpd) between eastward propagating wavenumbers 1-5. Holt et al. (2020) also found MJOs to
335 be simulated by these models in historical AMIP simulations (QBOi Exp 1). The highest MJO power in GPCP is concentrated
336 between wavenumbers 1 and 3 and exceeds that of ERA5 and the models. EC-EARTH3.3, MIROC-AGCM-LL, MIROC-
337 ESM, MRI-ESM2.0 correctly position MJO power between wavenumbers 1-3 whereas ECHAM5sh, EMAC (sharing
338 convective parameterizations) and LMDz6 exhibit spectral power that is incorrectly shifted towards higher wavenumbers. The
339 amplitude of the MJO is comparatively small in GISS-E2-2-G, LMDz6, and WACCM5-110L, which may adversely affect
340 their stratospheric waves, since these three models adopted interactive GW sources. The El Niño minus La Niña differences
341 in the rightmost column of Figure 2 show that MJO spectral power is stronger in the presence of the El Niño basic state.
342 Differing from the other models, EC-EARTH3.3, ECHAM5sh, and EMAC have fairly large El Niño minus La Niña MJO
343 power differences at wavenumber 4 and 5.

344
345 Irrespective of ENSO phase, the amplitude of the model MJOs as shown in Fig. 2 is systematically weaker than in GPCP or
346 ERA5. This may have something to do with dividing each simulation’s symmetric power by its respective background power,

347 the latter of which is contaminated, in a sense, by the perpetual ENSO conditions. Note that recomputing the third column of
348 Fig. 2 without dividing each El Niño and La Niña composite by their respective background does not change our conclusions
349 (not shown). To get around this potential issue with the background power and further inspect the model MJOs as opposed to
350 the convectively coupled waves, in Figures 3 we consider the westward and eastward wavenumber-frequency spectra of
351 U850 taken over the intraseasonal timescale and over MJO-like zonal wavenumber scales. These analyses yield more holistic
352 views of the MJO than in Fig. 2 because they incorporate the MJO's signals in these fields that are both symmetric and
353 antisymmetric about the equator.

354



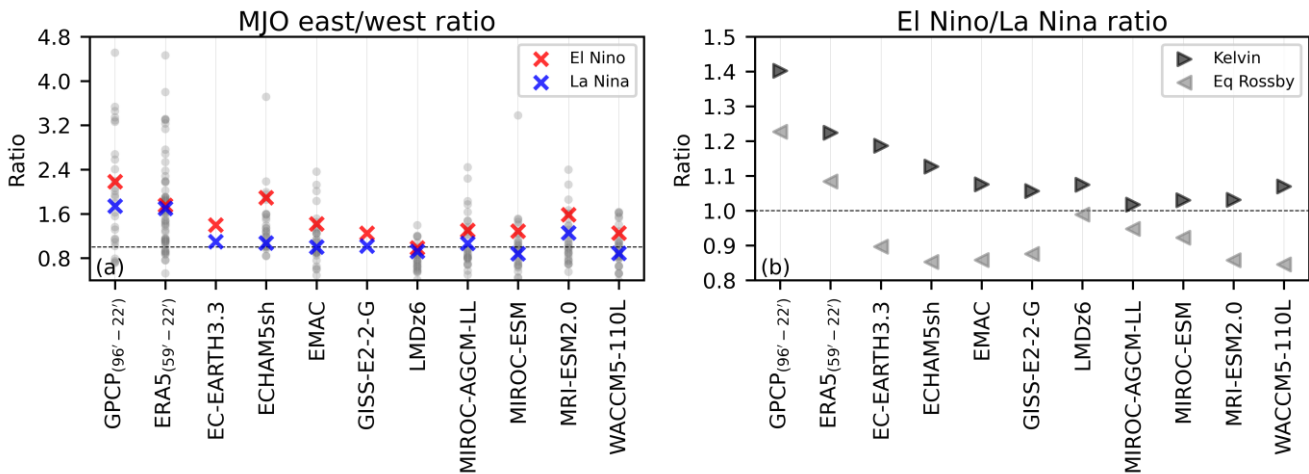
355
356
357
358
359
360
361

Figure 3: November-April wavenumber-frequency power spectra of 10°S-10°N averaged U850. Units of the U850 spectrum are m^2/s^2 per frequency interval per wavenumber interval. We interpret the power at ~ 180 -day frequencies as a by-product of using centered November-April segments.

As shown by ERA5, the MJO timescale variance of dynamical fields such as U850 are known to have a narrow spectral peak around zonal wavenumber-1 (Hendon and Salby 1994). The models are fairly good at reproducing this (Fig. 3), despite large

362 inter-model differences in terms of peak amplitudes. Independent of the ENSO phase, ERA5’s wavenumber-frequency shows
 363 the highest power between frequencies of 30-80 days (vertical dashes), a so-called “MJO band” (Ahn et al. 2017). Considering
 364 only the ERA5 MJO band, the MJO is stronger given lower zonal wavenumbers and longer periodicities during La Niña
 365 compared to El Niño. Similarly, the model spectra broadly indicates that the periodicity of the MJO decreases during El Niño
 366 and increases during La Niña. However, as was the case for the symmetric precipitation spectra (Fig. 2), there are notable
 367 differences in the amplitude of the spectral power between models and reanalysis. Of the models, MJO band amplitude in
 368 ECHAM5sh and EMAC is most like ERA5, whereas other models, particularly MIROC-AGCM-LL, MIROC-ESM, and
 369 GISS-E2-2-G significantly underestimate the strength of the MJO in this metric. Another issue is that models exhibit too large
 370 of an MJO signal for zonal wavenumbers three and up, which is unrealistic and common amongst GCMs (Ahn et al. 2017),
 371 with particularly exaggerated high-wavenumber amplitudes in ECHAM5sh, EMAC, and LMDz6, as previously noted for
 372 precipitation. The clustering of models related to each other, such as MIROC and ECHAM-based models, indicate that also
 373 the tropospheric wind response to imposed ENSO anomalies is strongly influenced by model configuration and convective
 374 schemes.

375
 376



377
 378

Figure 4: (a) Ratio of eastward to westward MJO precipitation spectral power (from Figure 2) filtered for wavenumbers +/- 1 to 3 and 30 to 96 day frequencies. Red and blue X's denote El Niño and La Niña, respectively, using the same notation for both the GPCP and ERA5 composite averages and the climatological values from the perpetual El Niño and La Niña simulations. Gray dots indicate interannual east/west ratios from GPCP, ERA5, and the QBOi Experiment 1 simulations (1979-2009 AMIP) by these same models; EC-EARTH3.3 and GISS-E2-2G did not run Experiment 1. (b) Ratio of Kelvin wave and equatorial Rossby wave power in El Niño to that in La Niña. Each wave is filtered using equivalent depths of 8 to 90 meters, with wavenumbers of 1 to 14 for the Kelvin wave and -1 to -10 for the equatorial Rossby wave.

385

386 To further explore the MJO timescale changes suggested by Figure 3, Figure 4a shows the ratio of eastward to westward MJO
 387 spectral power in symmetric precipitation from GPCP, ERA5, and the models. The E/W ratio measures how robust MJO
 388 eastward propagation is (Jiang et al. 2015; Ahn et al. 2017). El Niño and La Niña responses in GPCP and ERA5 (red and blue
 389 X's) are derived from composites of previously defined strong ENSO seasons, while gray dots represent interannual E/W
 390 ratios across all years (GPCP: 1996–2022; ERA5: 1959–2022), providing a baseline of internal variability. Both data sets show
 391 modestly higher E/W ratios during El Niño than La Niña.

392

393 While the model ENSO responses in Figure 4a are derived from climatological means of perpetual ENSO simulations, rather
 394 than event-based composites as in GPCP and ERA5, making direct comparison imperfect, the juxtaposition nonetheless reveals
 395 systematic differences in MJO behavior across observational and modeled frameworks. Model gray dots are interannual ratios
 396 from QBOi Experiment 1 AMIP 1979-2009 simulations, which contextualizes model internal variability. E/W ratios are higher
 397 in El Niño simulations, shifting towards the upper tail of the AMIP-based sampling variability. Conversely, many of La Niña
 398 E/W ratios are around one (dashed line), indicating subdued MJO propagation. The response to ENSO is relatively small in
 399 models with a weak MJO, such as GISS, LMDz6 and MIROC-AGCM-LL.

400

401 Building on the observed ENSO-related changes in MJO propagation, Figure 4b further quantifies how convectively coupled
 402 equatorial waves, Kelvin and equatorial Rossby, respond to ENSO forcing, given their known links to MJO variability. Figure
 403 4b shows the ratio of El Niño to La Niña precipitation-based spectral power, filtered from Figure 2 for each wave type. GPCP
 404 and ERA5 composites indicate that both waves are stronger during El Niño than La Niña. Models generally reproduce stronger
 405 Kelvin waves in their El Niño simulations, however, equatorial Rossby waves are consistently stronger during La Niña, in
 406 contrast to GPCP and ERA5. This disagreement between observational products and models regarding is difficult to attribute
 407 given the differences in how spectra for each are computed and known biases in modeled precipitation spectra (Holt et al.
 408 2020, Experiment 1). It appears to stem from a combination of model equatorial Rossby waves being underestimated in the
 409 El Niño simulation and overestimated relative to GPCP and ERA5 in the La Niña simulation (Fig. S2). Taken together, Figures
 410 3 and 4 suggest that MJO periodicity tends to shorten during El Niño and lengthen during La Niña. The robustness of this
 411 relationship is further assessed using Pohl and Matthews (2007) MJO statistics, including MJO lifetime, summarized in Table
 412 2.

413

414 *Table 2: The number of MJO events, their mean lifetimes and standard errors (reported in parentheses), and their mean amplitudes given*
 415 *either perpetual El Niño or La Niña conditions in a model. An asterisk (*) next to a model name indicates that the RMMs were retrieved*
 416 *using only 250 and 850 hPa zonal wind. Different from the models, for ERA5, MJO event statistics are calculated using 8 El Niño and 6 La*
 417 *Niña winters subsampled from the entire 1959-2022 RMM record.*

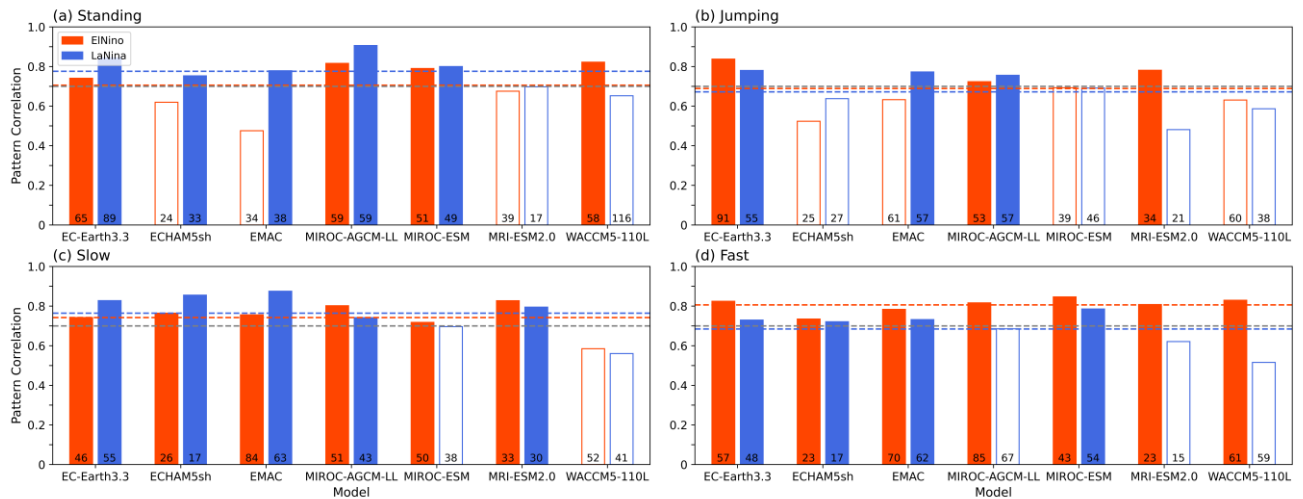
418

	EN events (#/dec)	LN events (#/dec)	EN lifetime (days)	LN lifetime (days)	EN amplitude	LN amplitude
ERA5	25	22	38.25 (2.27)	47.07 (3.97)	1.36	1.41
EC-EARTH3.3	18.07	13.80	37.96 (1.25)	46.73 (2.01)	1.47	1.40
ECHAM5sh	26.20	15.87	28.59 (1.18)	42.94 (3.26)	1.43	1.38
EMAC	23.83	14.75	29.77 (0.88)	45.57 (1.93)	1.37	1.45
GISS-E2-2-G*	20.56	11.46	32.23 (1.87)	37.06 (3.50)	1.42	1.31
LMDz6*	11.30	9.81	37.01 (2.20)	32.47 (1.69)	1.55	1.41

MIROC-AGCM-LL	23.48	19.26	30.31 (0.78)	30.90 (1.11)	1.46	1.49
MIROC-ESM	27.77	18.15	27.96 (0.57)	29.90 (1.15)	1.38	1.34
MRI-ESM2.0	21.53	16.70	35.02 (1.39)	39.35 (1.88)	1.43	1.40
WACCM5-110L	26.00	16.87	27.13 (0.77)	36.99 (1.31)	1.40	1.49

419 Based on ERA5, La Niña events are roughly nine days longer than El Niño events on average. Wei and Ren (2019) found La
420 Niña to support both high-frequency (lifetime ~40 days) and low frequency (lifetime ~80 days) MJOs, which conceivably
421 explains the much larger ERA5 lifetime standard errors during La Niña compared with El Niño. Strikingly, the difference in
422 lifetime and its standard error between ENSO phases is nearly ubiquitous across the models. With the exception of LMDZ6,
423 La Niña lifetimes are between 0.59 (MIROC-AGCM-LL) and 15.8 (EMAC) days longer than El Niño lifetimes. Models in
424 similar families, for instance ECHAM5sh and EMAC as well as MIROC-AGCM-LL and MIROC-ESM, typically have similar
425 magnitude differences in their Pohl and Matthews (2007) statistics between ENSO phases. All models simulate more MJO
426 events during El Niño, which is consistent with ERA5, however the difference in the number of events between ENSO phases
427 is generally larger in the models than in ERA5. MJO amplitude is only marginally larger during La Niña based on ERA5
428 whereas six of the nine models have larger amplitudes during El Niño.

430
431 Analyzing MJO diversity offers further insight into its propagation characteristics. K-means clustering of empirical OLR
432 Hovmöller diagrams reveals four dominant archetypes: standing, jumping, slow, and fast propagating MJOs (Wang et al.
433 2019). Associated SST composites show standing MJOs tend to coincide with La Niña, fast MJOs with El Niño, while jumping
434 and slow events show no clear ENSO linkage (Back et al. 2024). The experimental design allows us to test whether certain
435 archetypes become more robust under persistent ENSO forcing. Fast and slow events can occur during either ENSO phase
436 (Yadav and Straus 2017), suggesting some sensitivity of the established archetype-ENSO associations to internal variability.
437 Figure 5 lists the number of each archetype’s events simulated by each model (at the base of each bar). Standing and jumping
438 MJOs occur with similar frequency across ENSO phases, with four of seven models producing more standing events during
439 La Niña and four models producing more jumping events during El Niño, results that do not indicate a consistent ENSO
440 dependence. In contrast, slow and fast MJOs are modestly more frequent in El Niño simulations for six of seven models.

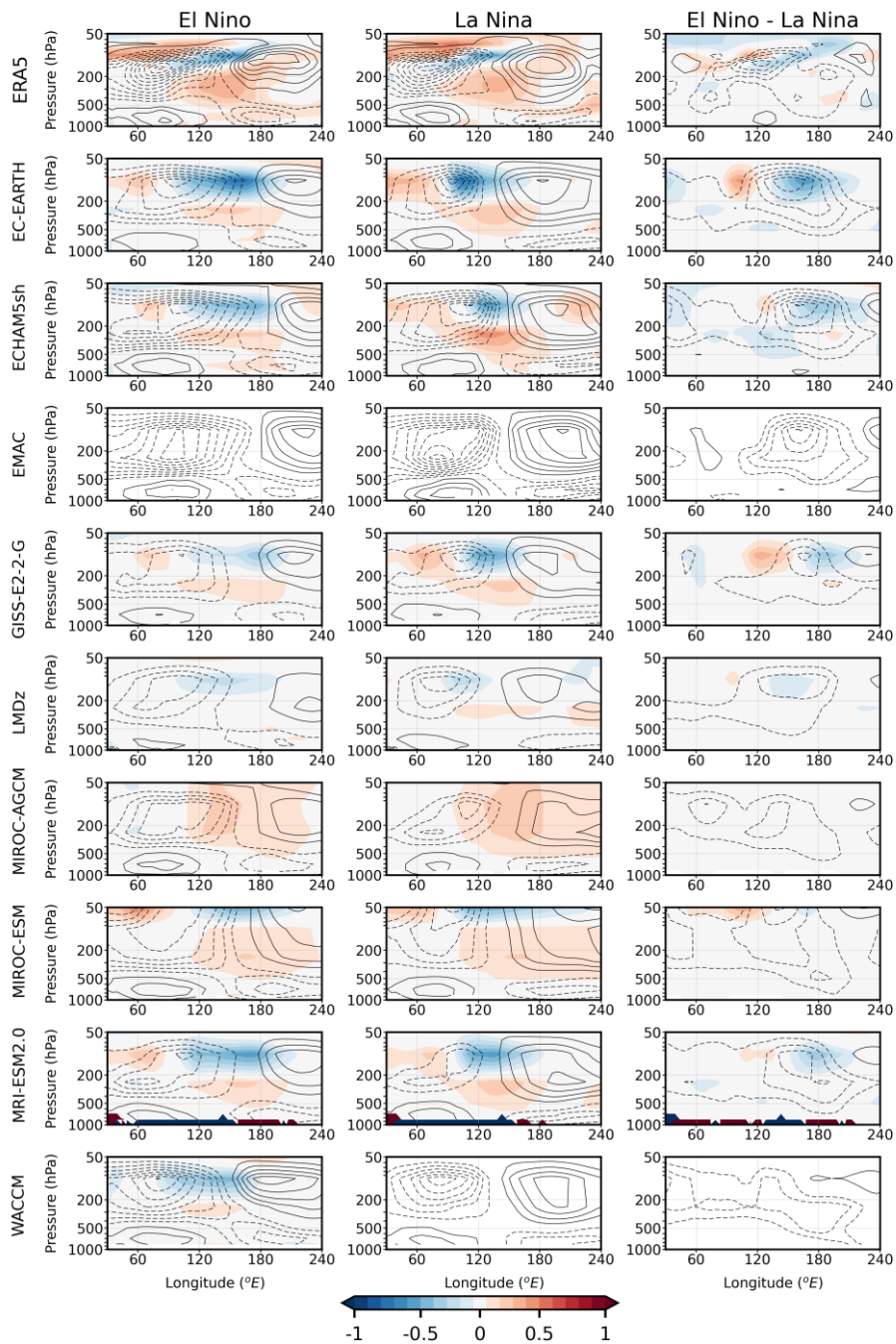


443 **Figure 5: Pattern correlations between the ERA5 and simulated time-longitude (Hovmöller) 10°S-10°N convective OLR anomaly**
 444 **composites (OLR < -5 W/m²) corresponding to each of the four K-means clusters MJO archetypes defined in Wang et al. (2019).**
 445 **Multi-model average El Niño and La Niña correlations are shown by red and blue dashed lines, and shaded (non-**
 446 **shaded) bars exceed (fall beneath) these multi-model means. The gray dashed line marked at a correlation of 0.7 is a heuristic**
 447 **threshold (Back et al. 2024) to decide when a particular model’s MJO archetype is well captured by a model. Number of events is**
 448 **printed at the bottom of each bar.**
 449
 450

451 To assess how closely model archetypes resemble those in reanalysis, we calculate pattern correlations between ERA5 and
 452 model time-longitude tropical OLR anomaly composites for each cluster. This evaluates how well models capture observed
 453 MJO archetypes and whether representation improves under ENSO forcing. Prior multi-model studies (Back et al. 2024)
 454 suggest a pattern correlation of 0.7 as a threshold for distinguishing well-simulated OLR Hovmöllers. For the standing MJO
 455 (Fig. 5a), five of 14 models fall below this threshold and are shaded white. Although roughly a third of simulations poorly
 456 represent the standing cluster, model skill improves during La Niña, with the multi-model mean correlation exceeding the El
 457 Niño value by 0.09. For jumping MJOs (Fig. 5b), correlations fall below 0.7 in over half the models, indicating widespread
 458 difficulty in simulating this archetype. As jumping MJOs are not thought to be ENSO-sensitive, they are not analyzed further.
 459 Studies suggest slowly propagating MJOs often coincide with La Niña, though the associated SST pattern is weak and
 460 statistically insignificant (Wang et al. 2019; Back et al. 2024). Similarly, model skill is slightly higher in La Niña simulations,
 461 but likely indistinguishable from El Niño (Fig. 5c). In contrast, fast MJOs are better represented in every El Niño simulation,
 462 with the multi-model mean correlation exceeding the La Niña mean by 0.11 (Fig. 5d). In summary, model skill in representing
 463 fast and standing MJOs tends to be higher during El Niño and La Niña simulations, respectively, and models simulate a
 464 modestly higher number of fast events in their El Niño simulation
 465

466 The vertical structure of the MJO differs between slow and fast propagating events (Wang et al. 2019). To consider this further,
 467 we regress the latitudinally averaged 10°S-10°N zonal wind and temperature from ERA5 and the models onto their phase 3/4
 468 RMM indices as in Hendon and Abhik (2018) and form pressure-longitude cross-sections (Figure 6). Phases 3/4, when the
 469 MJO convection is over the western Maritime Continent, are of interest because ENSO modulates the low-frequency

470 circulation here through its effect on the Walker Circulation, giving it a pathway to influence MJO propagation (Sun et al.
 471 2019; Suematsu and Miura 2022). Irrespective of the ENSO phase, the MJO in ERA5 exhibits a quadrupole structure in zonal
 472 wind, all of which is centered around a tropospheric warming at 140°E that peaks in amplitude near 300 hPa (cf. Jiang et al.
 473 2015).
 474



475

476 **Figure 6: Pressure-longitude cross-sections of the 10°S-10°N zonal wind and temperature regressed onto the Phase 3/4 RMMs as in**
477 **Hendon and Abhik (2018). Black contours show zonal wind (intervals of +/- 0.5, 1.5, 2.5 m/s...) and temperature is shaded between**
478 **-1 and 1 °C. EMAC is missing temperature and we omit WACCM's La Nina temperature due to a conspicuous artifact.**
479

480 Although the ERA5 El Niño and La Niña composites are similar overall, subtracting the two reveals that they differ due to the
481 El Niño composite including a stronger Kelvin wave, evidenced by the stronger tropospheric easterlies to the east of MJO
482 convection (cf. Fig. 2). In addition, the composites reveals a dry Kelvin wave signature, its characteristic features being a cold
483 cap temperature anomaly in the UTLS, which is slightly out of phase with easterly zonal wind anomalies, all of which tilt
484 eastward with increasing height above ~200 hPa and westward with increasing height below (Straub and Kiladis 2002; Kim
485 et al. 2013; Yuni et al. 2019; Nakamura and Takayabu 2022). Judging by the longitude of the ERA5 100 hPa cold cap maximas,
486 the dry Kelvin wave embedded in the composite El Niño MJO is shifted further east compared to its La Niña equivalent..
487

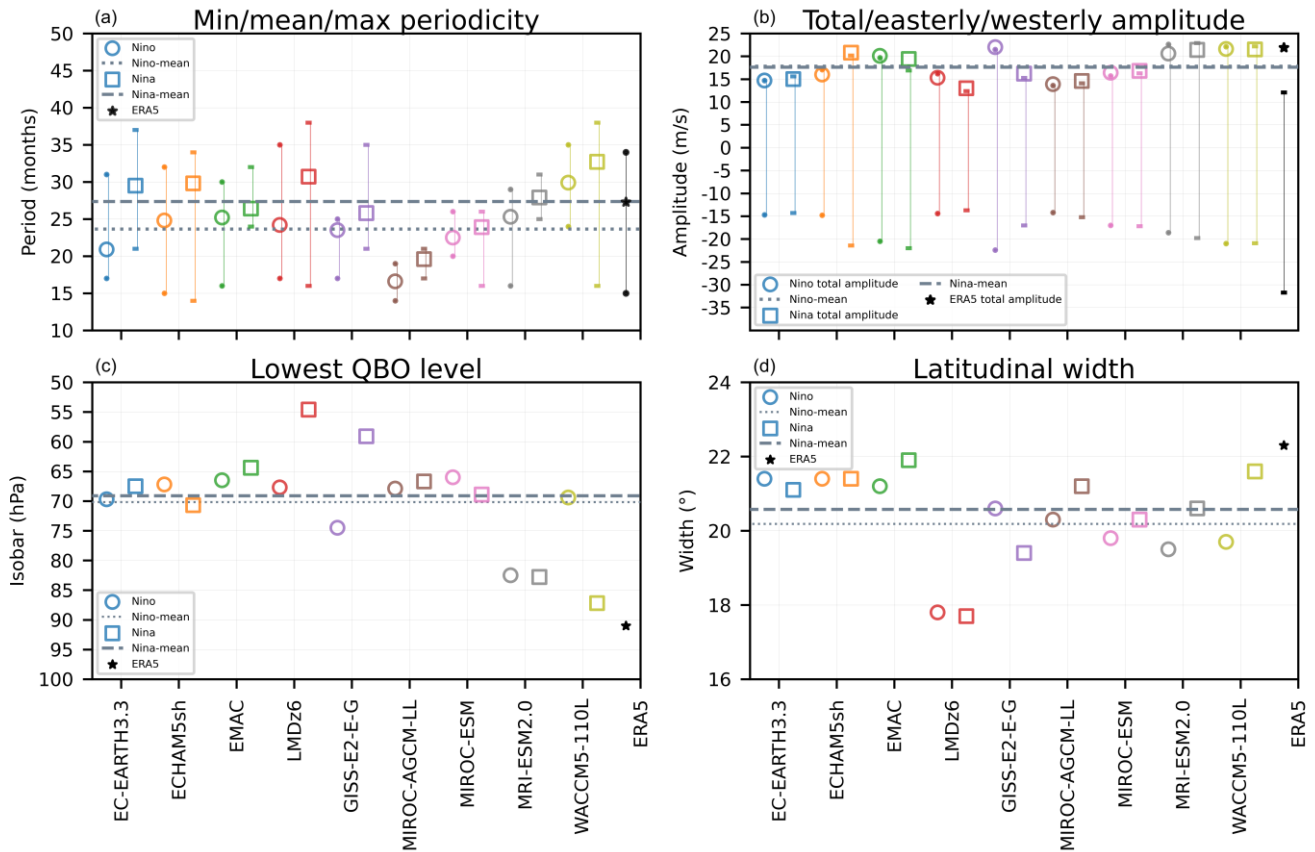
488 Consistent with recent studies, the surface easterlies positioned east of the MJO convection are indeed stronger during El Niño
489 in reanalysis (Wang et al. 2019; Wei and Ren 2019). We attribute the amplification of these easterlies to the Kelvin wave's
490 signature in wind, which better bridges the MJO lower tropospheric easterlies over the Pacific with the upper tropospheric
491 easterly outflow over the Indian Ocean; compare the 500 hPa zonal winds at 150°E between El Niño and La Niña. This
492 enhanced continuity of the MJO easterlies during El Niño is a robust feature amongst the models and is particularly clear in
493 the El Niño minus La Niña composites of EC-EARTH3.3, ECHAM5sh, MIROC-AGCM-LL, MIROC-ESM and MRI-
494 ESM2.0.
495

496 The vertical structure of the MJO zonal wind anomalies is more baroclinic during La Niña. This may be attributed to a weaker
497 and slower propagating Kelvin wave during La Niña. However, it is also possible that the amplification of the equatorial
498 Rossby wave during La Niña (cf. Figure 2) projects onto the MJO's vertical structure. For instance, similar to the western
499 portion of the phase 3/4 MJO winds, these waves (when located in the eastern hemisphere) have a first baroclinic structure in
500 zonal wind that consists of low-level westerlies and upper-level easterlies (Kiladis et al. 2009; Yuni et al. 2019; Nakamura and
501 Takayabu 2022). Following from the robust amplification of the equatorial Rossby wave across the models during La Niña, it
502 was hypothesized that the low-level westerlies west of the MJO convection would be stronger during La Niña than El Niño
503 like in Wei and Ren (2019). This does not appear to be the case though and no first baroclinic zonal wind structure stands out
504 in the El Niño minus La Niña composites. The signal of the equatorial Rossby wave does, however, appear to be visible in the
505 temperature field. These waves are associated with a mid to upper tropospheric warming that is centered around 300 hPa
506 (Kiladis et al. 2009, Fig. 18c). This region of the upper troposphere is warmer in all of the La Niña simulations, with the
507 exception of MIROC-ESM in which the warming is marginally stronger in the El Niño composite.

508 **3.2 The lack of QBO-MJO interaction**

509 The results in the previous section indicate that ENSO modulates the MJO's propagation, promoting faster MJOs during El
510 Niño and the opposite during La Niña. However, it is possible that aliased signals from the spontaneously generated QBOs are

511 embedded in the aforementioned results. Therefore, in this section we look for evidence of QBO-MJO interaction. As a first
 512 step, the representation of the QBO is documented using previously defined metrics, with a specific interest in quantifying the
 513 “lowest level” that the QBO descends to in the lower stratosphere. Insufficient descent is a known bias, which may hinder the
 514 QBO from modulating other potentially important variables near the tropopause such as temperature (Richter et al. 2020; Kim
 515 et al. 2020). Similar to Schenzinger et al. (2017), the lowest level that QBO reaches is found by averaging the QBO Fourier
 516 amplitude (see Methods) over 5°S-5°N, identifying the maximum amplitude (fixed at 20 hPa here), and then finding the isobar
 517 in the lower stratosphere where the amplitude equals 10% of the maximum.
 518



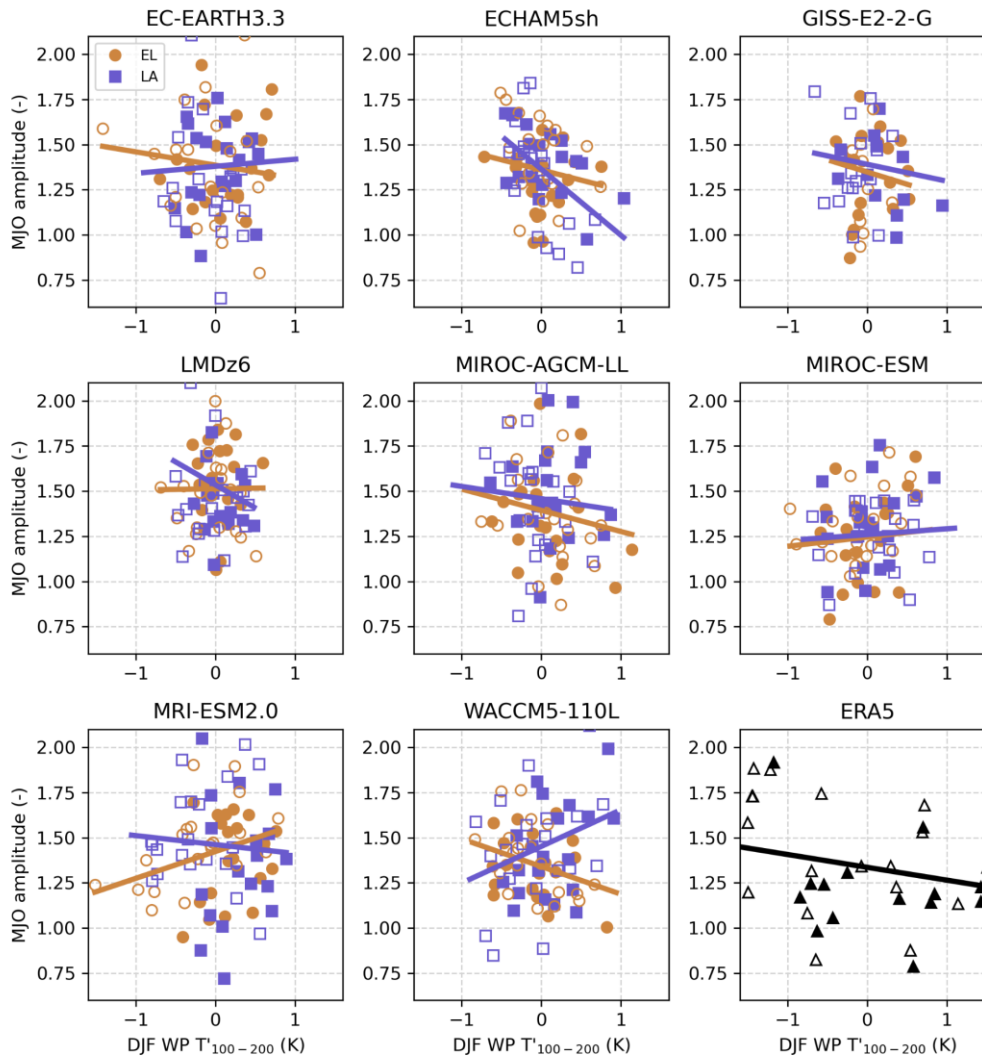
519
 520 **Figure 7: Periodicity, amplitude, lowest level of descent, and latitudinal width of the QBO in El Niño (circles) and La Niña (squares)**
 521 **simulations. (a) mean periodicity, where whiskers extend to the minimum and maximum period, El Niño mean is dotted, La Niña**
 522 **mean is dashed, and ERA5 is shown in black. (b) circles and squares show total amplitudes (“TT amplitude” from Richter et al.**
 523 **2020), tops of whiskers show westerly amplitudes, and bottoms of whiskers show easterly amplitudes. (c) lowest isobar the QBO**
 524 **descends to, the level at which the QBO Fourier amplitude falls to 10% of its maximum. (d) latitudinal width of QBO, full width at**
 525 **half amplitude maximum of a Gaussian fit to the QBO Fourier amplitude**
 526

527 The QBO descends to 92.2 hPa in ERA5 (Fig. 7c). Of the simulated QBOs, the majority do not reach beneath 70 hPa, indicating
528 that they are likely too high in altitude to influence the tropical atmosphere beneath 100 hPa as observed (Tegtmeier et al.
529 2020). One outlier is the WACCM5-110L's La Niña simulation whose lowest isobar of 87 hPa is fairly similar to the ERA5
530 benchmark. Nonetheless, sensitivity tests with this simulation in which MJO amplitude is computed as a function of lower
531 stratospheric QBO phase reveals its MJO to be insensitive to the QBO in the observed way (not shown), which may also be
532 attributable to the weak MJO signal in the model. ENSO phase does not have consistent effects on what lowest isobar a given
533 model's QBO reaches. For example, GISS-E2-2-G and LMDz6 favor much stronger descent of the QBO into the lower
534 stratosphere during El Niño whereas WACCM5-110L's ENSO simulations reflect a strong opposite signed response.

535
536 QBO periodicity varies systematically with ENSO phase in these simulations, being shorter during La Niña and longer during
537 El Niño (Fig. 7a); see Kawatani et al. (2025) for a detailed analysis of this result. However, none of the QBO spatial metrics
538 exhibit consistent ENSO-phase dependence across models. For example, total QBO amplitude is marginally stronger during
539 La Niña in five of the nine models (Fig. 7b). El Niño and La Niña total QBO amplitudes differ by less than 1 m/s for all models
540 except ECHAM5sh, GISS-E2-2-G, and LMDz6. ECHAM5sh favors a stronger QBO amplitude during La Niña, owing to
541 intensified QBO easterlies and westerlies during this ENSO phase. Conversely, GISS-E2-2-G, and LMDz6 favor stronger
542 easterly, westerly, and total QBO amplitudes during El Niño. Of the 12 simulations corresponding to the six other models, EC-
543 EARTH3.3, EMAC, MIROC-AGCM-LL, MIROC-ESM, MRI-ESM2.0, and WACCM5-110L, the magnitude of their easterly
544 and westerly QBO amplitudes is stronger during La Niña in eight of the 12 simulations. Although the models ubiquitously
545 underestimate the latitudinal extent of the QBOs relative to ERA5, six of nine models have wider QBO latitudinal extents
546 during La Niña (Fig. 7d). This may be noteworthy because the boreal winter polar stratospheric wind response to the QBO is
547 stronger when the QBO is wider (Hansen et al. 2013) and there is a preference for this teleconnection to happen during La
548 Niña over the observed record (Kumar et al. 2022).

549

550

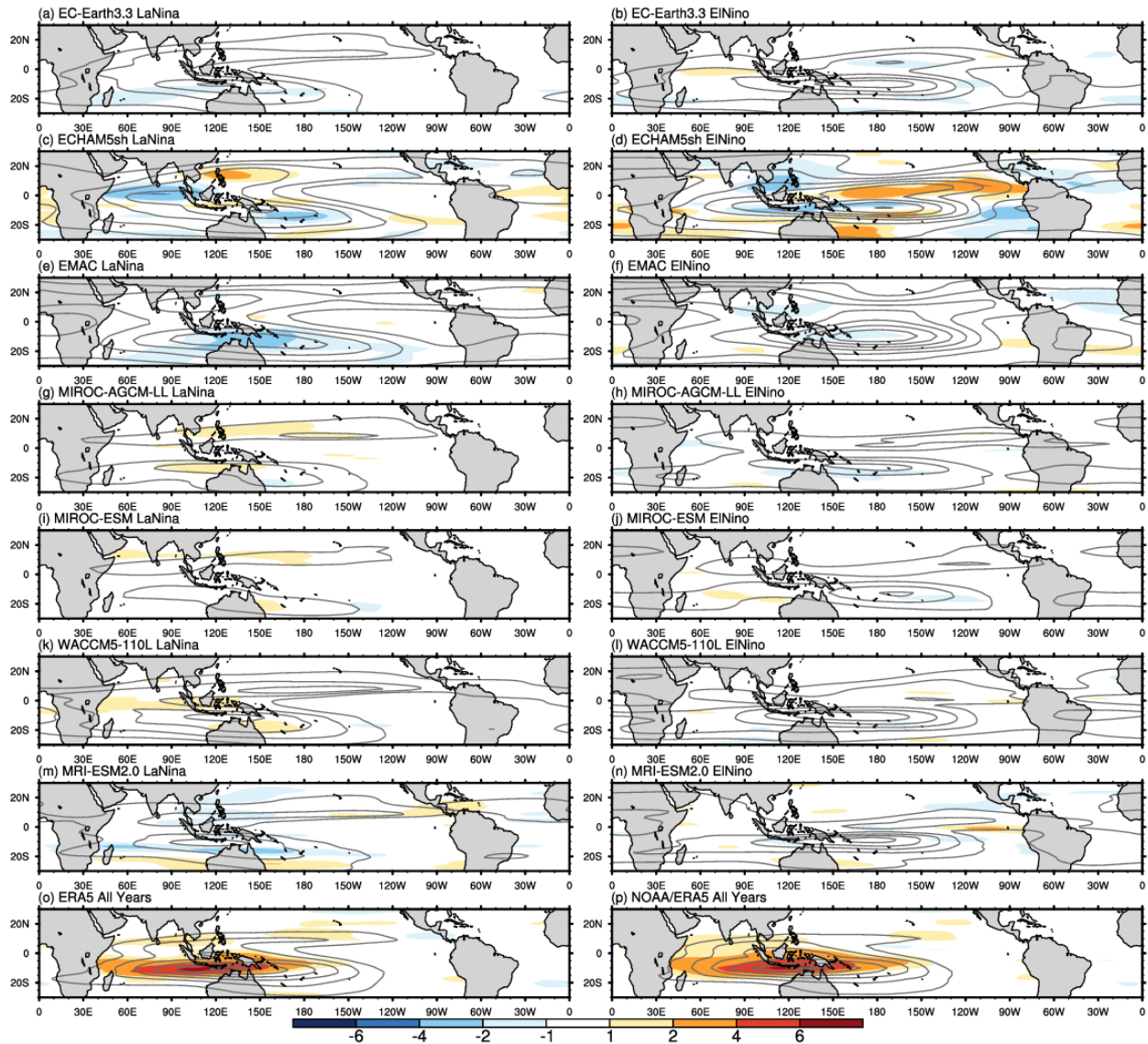


551
 552 **Figure 8:** Scatter plot of warm-pool averaged (10°S - 10°N , 45°E - 180°E) tropopause stability anomalies (100 hPa minus 200 hPa
 553 temperature) versus December-February MJO amplitude. Lines represent the slope of the regression line during El Niño (orange)
 554 or La Niña (purple). Easterly and westerly QBO phases, which are delineated by the sign of the December-February 5°S - 5°N 50 hPa
 555 zonal mean zonal-wind, are denoted by open and filled markers, respectively.
 556

557 While the aforementioned QBO metrics help to broadly characterize the form of each model's QBO, they are non-time-varying
 558 quantities and have less value for better understanding seasonal phenomena such as the predominantly boreal winter QBO-
 559 MJO interaction. To incorporate the effects of seasonality, scatterplots of December-February warm-pool averaged tropopause
 560 stability versus December-February MJO amplitude are made as a function of QBO phase for each of the simulations
 561 (Klotzbach et al. 2019). MJO amplitude is expected to increase as tropopause stability decreases (Son et al. 2017; Klotzbach
 562 et al. 2019), as is apparent based on ERA5 (Fig. 8). This metric is relevant for considering QBO-MJO coupling because the
 563 QBO's effect on lower stratospheric stability (e.g., Densmore et al. 2019) is one of the suspected physical mechanisms coupling

564 the QBO and MJO. In general, the models do not reproduce the observed inverse relation between MJO amplitude and 100-
565 200 hPa stability and stratifying the results either by ENSO phase or QBO phase does not change this. The linear response of
566 the MJO amplitude to the tropopause stability, which is negative in observations, does not change consistently with the ENSO
567 phase. It is worth noting that the mean DJF stability in the models is generally close to that of ERA5 (-28.7 K) except for the
568 GISS model, which showcases a smaller gradient (-23.3 K), and all models appear to underestimate its interannual variability,
569 as evident by the smaller range compared to ERA5 (recall however that imposed SSTs do not vary interannually). Furthermore,
570 the stratification by QBO phase (with EQBO associated with lower stability values, and vice versa for the WQBO) is also
571 small or absent in models, possibly due to a limited influence of the QBO at tropopause heights (Serva et al., 2022). Further
572 sensitivity tests were done to see if the model QBOs simulate a QBO-MJO amplitude relationship when the MJO is in a
573 particular phase (e.g., Lim and Son 2020; Lawrence et al. 2023); no systematic effect was detected (not shown).

MJO Activity (OLR σ)



574
575 **Figure 9:** Gray contours show the MJO activity defined as the standard deviation of MJO-filtered OLR for each model and ENSO
576 phase, as well as for ERA5 (6n). The color-filled contours show the MJO-QBO relationship as the difference in MJO activity for the
577 eastward minus westward 50 hPa QBO phases for each model and ERA5.
578

579 To further evaluate the representation of QBO-MJO coupling in the models, Figure 9 presents the effect of QBO phase on
580 MJO activity (see Methods). As shown in previous studies (e.g., Kim et al. 2020), the models do not capture the observed

581 QBO-MJO relationship, which has maximum signal over the maritime continent region (Fig. 9m) illustrating the enhancement
582 of MJO activity during easterly QBO phase. With La Niña forcing, MIROC-AGCM-LL and WACCM5-110L show a weak
583 positive signal over the Maritime Continent (Fig. 9g, k), however EC-EARTH3.3, ECHAM5sh, and EMAC exhibit rather
584 different responses. In MIROC models, the MJO activity is further shifted off-equator, possibly hampering any QBO control
585 on MJO convection. No change in the MJO activity by QBO phase is evident in the El Niño simulations either, except for
586 some negative signal in the central and eastern Pacific in ECHAM5sh, which may be due to an irregular QBO in this experiment
587 (Kawatani et al., 2025). There is, however, a clear eastward shift of the MJO activity towards the Pacific during El Niño,
588 corroborating the observational work of Kessler (2001) and the climate model based study of Tam and Lau (2005).

589 **4 Discussion and conclusions**

590 The observed interannual variability of the MJO is influenced by multiple parts of the climate system. Due to their impact on
591 the tropical troposphere and prominent fluctuations at interannual timescales, ENSO and the QBO are known drivers of the
592 MJO's year to year variability, however it is difficult to definitively isolate their influence on the MJO because of how short
593 and noisy the observational record is (Randall et al. 2023). Building on previous work, our aim here is to evaluate the extent
594 to which model behavior is consistent with previously reported ENSO-MJO relationships by analyzing the representation of
595 the MJO in nine climate models forced by prescribed perpetual El Niño and La Niña conditions, each with a spontaneously
596 generated QBO. While the imposed SST anomalies represent an upper bound for the observed record, they are relevant given
597 the projected intensity increase of ENSO extremes.

598
599 Although the models exhibit difficulties simulating the MJO, several previously reported effects of the ENSO phase on the
600 MJO are corroborated by this coordinated set of experiments. These effects include faster propagation of the MJO during El
601 Niño versus slower propagation during La Niña, manifesting as shorter and longer lifetimes, respectively, stronger amplitude
602 of the MJO during El Niño, and east-west shifting of the MJO timescale variance towards the east Pacific during El Niño and
603 towards the west Pacific and Indian Ocean during La Niña. It is likely that the high-amplitude SST forcings used here,
604 particularly the amplified El Niño forcing, contribute to the magnitude of these ENSO associated MJO changes, consistent
605 with prior work linking exceptionally warm Pacific SSTs to enhanced or farther-east MJO propagation (e.g., Marshall et al.
606 2016). To assess this sensitivity to ENSO amplitude, we compare a broad measure of MJO quality and propagation, the MJO
607 E/W ratio, between the perpetual ENSO simulations and each model's 1979–2009 AMIP simulations, which are more
608 representative of typical ENSO amplitudes. Across models, El Niño forcing increases the E/W ratio, often pushing it toward
609 the upper tail of the AMIP-based internal variability distribution, indicating more robust eastward MJO propagation, whereas
610 many La Niña simulations produce ratios near unity. Notably, all perpetual ENSO E/W ratios remain within the spectrum of
611 their AMIP-based values, underscoring that the modeled responses, while produced by extreme forcings, do not exceed the
612 range of variability seen under more normal SSTs. We note that, besides SSTs, the representation of MJOs in models appears
613 to be particularly sensitive to convective schemes, as discussed by Rind et al. (2020) for GISS, by Park et al. (2019) for

614 WACCM, by Miura et al. (2012) for MIROC and Holt et al. (2020) for other Phase 1 QBOi models. The impact of the
615 convective scheme, for example, appears oversized compared to horizontal resolution, which is finely resolved in EC-
616 EARTH3.3, MIROC-AGCM-LL, MRI-ESM2.0, and WACCM, none of which are exceptional at reproducing the MJO's
617 wavenumber frequency spectra or E/W ratios. Moreover, models within the same family (MIROC-based, ECHAM-based)
618 exhibit similar MJO spectra (Fig. 2, Fig. 4), despite having intra-family differences in horizontal and vertical resolution (Table
619 2; Holt et al. 2020, Fig. 18). As shown by Orbe et al. (2020) for the WACCM and GISS models, refinement of key
620 parameterization has potential to improve simulated MJOs.

621

622 As in the observational record, it is possible that aliasing from the QBO is superimposed on what are thought to be MJO
623 changes due to ENSO. However, we find that the climate models considered here show little evidence of QBO-MJO coupling.
624 This may be due to various factors, such as biases in the descent of the QBO, and the location and characteristics of tropical
625 convection, which appears to be less organized in some of the models compared to GPCP. While this limits our ability to
626 diagnose the mechanisms linking the QBO and MJO, it suggests that, in these experiments, the MJO changes we detect are
627 primarily driven by the ENSO forcings. Experiments with specified rather than internally generated QBO aspects can help
628 understanding the processes at play, which remain elusive (Martin et al., 2023; Huang et al. 2023). One speculative reason for
629 the missing QBO-MJO signal is the representation of Kelvin waves. Observations show that during EQBO, the Kelvin wave
630 associated with MJO penetrates higher into the lower stratosphere, coinciding with an eastward-tilting cold anomaly in the
631 UTLS (Hendon and Abhik 2018). We find a similar dry Kelvin wave signature in our ERA5 El Niño minus La Niña MJO
632 vertical structure composite, but in models, the UTLS wave structure is much more coarsely resolved (Fig. 6). Such
633 deficiencies, perhaps linked to vertical resolution (Holt et al. 2020, Fig. 18a), lower-stratospheric wind biases that develop in
634 the absence of sufficient QBO descent (Fig. 7c), or perhaps just weak MJOs, may weaken this dry Kelvin wave component
635 and, in turn, suppress QBO-MJO interaction.

636

637 These results highlight that the interannual variability of the MJO is sensitive to ENSO in several regards, in contrast with
638 Slingo et al. (1999) and Hendon et al. (1999). These studies reported a weak simultaneous relationship between ENSO and
639 MJO activity. Hendon et al. (1999) found that increased MJO activity coincides with an increased number of MJO events and
640 enhanced intraseasonal convective activity around the Maritime Continent. While these attributes of the MJO were largely
641 insensitive to SSTs in their study, the models here unambiguously simulate more events in their perpetual El Niño simulation
642 (Table 2), which are of stronger MJO activity than their La Niña equivalents (Figure 8). We suspect that the distinction between
643 our results and the previous research is related to the timescale over which the oceanic component of ENSO modulates the
644 atmosphere. Recent studies show that while the likelihood of MJO occurrence and its propagation speed are only weakly
645 correlated with tropical intraseasonally filtered SSTs, they are strongly correlated with low-frequency (e.g., > 90 days) SSTs
646 (Suematsu and Miura 2018; 2022). Along the same lines, Newman et al. (2009) found air-sea coupling to have weak effects
647 on subseasonal atmospheric variability, but strong influence on the long-term atmospheric circulation. In light of this and our
648 use of a simplified climate system in which smoothed monthly SSTs are prescribed, intraseasonal and interannual SST

649 fluctuations are explicitly ignored, and the downward impact of the MJO on intraseasonal SSTs (Zhang and Gottschalk 2002;
650 Hendon et al. 2007; Newman et al. 2009) is not simulated, we deduce that the different basic state circulations set up by the
651 indefinite ENSO forcings enables distinct MJOs. This interpretation of the low-frequency SSTs as an important modulator of
652 the MJO aligns with studies which have attributed variability in the MJO's propagation to ENSO (Wei and Ren 2019; Wang
653 et al. 2019; Dasgupta et al. 2021; Back et al. 2024) as well as studies employing climate models in which MJO propagation
654 can be modulated by changing the horizontal gradients of the background SST field (Kang et al. 2013; Jiang et al. 2020).

655
656 Compared with the La Niña simulations, all El Niño simulations include amplified Kelvin waves whereas equatorial Rossby
657 waves intensify in the presence of perpetual La Niña conditions. Consistent with the reported relationship between the these
658 wave and the MJO (Wei and Ren 2019), all models simulate faster MJO propagation in their El Niño simulation. This is further
659 supported by the MJO diversity analysis, which reveals that models reproduce the observed fast and standing MJO archetype
660 OLR Hovmöllers well in the presence of perpetual El Niño and La Niña conditions, respectively. In addition, the MJO's phase
661 3/4 vertical structures highlight that lower tropospheric easterlies do intensify to the east of the MJO's major convection during
662 El Niño across most models, which we interpret to result from the intensification of the Kelvin wave.

663
664 While the relationship between Kelvin waves, equatorial Rossby waves, and ENSO is well established by previous studies
665 employing empirical data and reanalysis, this is the first time, to the best of our knowledge, that this relationship has been
666 ubiquitously affirmed by a coordinated set of climate model experiments with prescribed strong ENSO forcings. The
667 robustness of this result across models suggests that it is worthwhile considering how these wave responses to ENSO influence
668 other parts of the climate system. For instance, Kelvin waves are a source of resolved wave forcing for the QBO (Baldwin et
669 al. 2001; Taguchi 2010; Pahlavan et al. 2021) and more rapid descent of the QBO's westerly shear zones during El Niño in
670 observations has been attributed to their intensification (Das and Pan 2016). The periodicity of the QBO in the El Niño
671 simulations is in fact shorter than in the La Niña simulations across all models considered here (Kawatani et al., 2025),
672 however, the extent to which Kelvin waves are responsible for this as opposed to other waves (e.g., Kawatani et al. 2019), is
673 yet to be quantified across all of the models. The convectively coupled wave responses presented here may also be relevant
674 for better understanding ENSO diversity. El Niño events vary in type and intensity due to the influence of westerly wind bursts,
675 which introduce asymmetry and irregularity into ENSO's phase changes (Chen et al. 2015). Westerly wind bursts are more
676 frequent during the convective phases of equatorial Rossby waves and the MJO, especially strong MJOs (Puy et al. 2016).
677 Hence, the atmospheric responses to ENSO, such as the amplifications of the MJO during El Niño (Figs. 2-4) and of the
678 convectively coupled Rossby wave during La Niña, have a pathway to influence ENSO's oceanic component.

679 680 **Code availability**

681
682 The code used for the wavenumber-frequency analysis is publicly available through the National Center for Atmospheric
683 Research (NCAR) Command Language (NCL): <https://www.ncl.ucar.edu/Applications/mjoelivar.shtml>. A reproduction of

684 NCL's Wheeler-Kiladis (1999) routine in Python is available here: https://github.com/brianpm/wavenumber_frequency.
685 Python code, which assesses QBO morphology is available here: [https://github.com/NOAA-GFDL/MDTF-](https://github.com/NOAA-GFDL/MDTF-diagnostics/blob/main/diagnostics/stc_qbo_enso/stc_qbo_enso.py)
686 [diagnostics/blob/main/diagnostics/stc_qbo_enso/stc_qbo_enso.py](https://github.com/NOAA-GFDL/MDTF-diagnostics/blob/main/diagnostics/stc_qbo_enso/stc_qbo_enso.py).

687

688 **Data availability**

689 Storage for the QBOi multi-model data set is provided by the Centre for Environmental Data Analysis (CEDA) whose data
690 and processing service is called JASMIN. Interested users must obtain a JASMIN login account and take the necessary steps
691 to access the QBOi group workspace within JASMIN, which contains the perpetual ENSO simulations. Certain derived model
692 products (e.g., the MJO RMMs) may be made available upon request.

693

694 **Author contributions**

695 DE, FS, JC, SYB, CO, and JR contributed to the conceptualization of this study. DE, FS, JC, and SYB performed the data
696 analyses and produced the figures and tables. All authors contributed to the review and editing of this manuscript.

697

698 **Competing interests**

699 The authors declare that they have no conflict of interest.

700

701 **Acknowledgements**

702 DE was supported in part by NOAA Cooperative Agreement NA22OAR4320151 and appreciates helpful discussions with
703 John Albers, Juliana Dias, George Kiladis, Matthew Newman, Brandon Wolding, and Amy Butler. The ECHAM5sh
704 simulations were performed thanks to an ECMWF Special Project awarded to FS. YK[KY1] was supported by JSPS
705 KAKENHI (JP22K18743) and the Environment Research and Technology Development Fund (JPMEERF20242001) of the
706 Environmental Restoration and Conservation Agency provided by Ministry of the Environment of Japan. YK and SW were
707 supported by JSPS KAKENHI (JP22H01303 and JP23K22574). SW was supported by MEXT-Program for the advanced
708 studies of climate change projection (SENTAN) Grant Number JPMXD0722681344. S.-W. Son was supported by a grant
709 from the National Research Foundation of Korea (NRF), funded by the Korean government (MSIT) (2023R1A2C3005607).
710 NB was funded by the Met Office Climate Science for Service Partnership (CSSP) China project under the International
711 Science Partnerships Fund (ISPF). The numerical simulations of MIROC models were performed using the Earth Simulator.
712 The GFD-DENNOU Library and GrADS were used to draw the figures. TK and SV acknowledge support by the state of
713 Baden-Württemberg through bwHPC. Portions of this work were supported by the National Center for Atmospheric Research
714 (NCAR), which is a major facility sponsored by the National Science Foundation (NSF) under Cooperative Agreement
715 1852977. Portions of this study were supported by the Regional and Global Model Analysis (RGMA) component of the Earth
716 and Environmental System Modeling Program of the U.S. Department of Energy's Office of Biological and Environmental
717 Research (BER) via NSF Interagency Agreement 1844590. The authors gratefully acknowledge the UK Centre for
718 Environmental Data Analysis for providing archival and analysis resources for the QBOi multimodel dataset.

720 **References**

721

722 Adler, Robert; Wang, Jian-Jian; Sapiano, Mathew; Huffman, George; Bolvin, David; Nelkin, Eric; and NOAA CDR Program
 723 (2017). Global Precipitation Climatology Project (GPCP) Climate Data Record (CDR), Version 1.3 (Daily) [1996-2022].
 724 NOAA National Centers for Environmental Information. doi:10.7289/V5RX998Z [July 2025]

725

726 Ahn, M.-S., Kim, D., Sperber, K. R., Kang, I.-S., Maloney, E., Waliser, D., and Hendon, H.: MJO simulation in CMIP5 climate
 727 models: MJO skill metrics and process-oriented diagnosis, *Clim Dyn*, 49, 4023–4045, [https://doi.org/10.1007/s00382-017-](https://doi.org/10.1007/s00382-017-3558-4)
 728 [3558-4](https://doi.org/10.1007/s00382-017-3558-4), 2017.

729

730 Ahn, M., Kim, D., Kang, D., Lee, J., Sperber, K. R., Gleckler, P. J., Jiang, X., Ham, Y., and Kim, H.: MJO Propagation Across
 731 the Maritime Continent: Are CMIP6 Models Better Than CMIP5 Models?, *Geophysical Research Letters*, 47,
 732 e2020GL087250, <https://doi.org/10.1029/2020GL087250>, 2020.

733

734 Back, S.-Y., Kim, D., and Son, S.-W.: MJO Diversity in CMIP6 Models, *Journal of Climate*, 37, 4835–4850,
 735 <https://doi.org/10.1175/JCLI-D-23-0656.1>, 2024.

736

737 Baldwin, M. P., Gray, L. J., Dunkerton, T. J., Hamilton, K., Haynes, P. H., Randel, W. J., Holton, J. R., Alexander, M. J.,
 738 Hirota, I., Horinouchi, T., Jones, D. B. A., Kinniersley, J. S., Marquardt, C., Sato, K., and Takahashi, M.: The quasi-biennial
 739 oscillation, *Reviews of Geophysics*, 39, 179–229, <https://doi.org/10.1029/1999RG000073>, 2001.

740

741 Bechtold, P., Semane, N., Lopez, P., Chaboureaud, J.-P., Beljaars, A., and Bormann, N.: Representing Equilibrium and
 742 Nonequilibrium Convection in Large-Scale Models, *Journal of the Atmospheric Sciences*, 71, 734–753,
 743 <https://doi.org/10.1175/JAS-D-13-0163.1>, 2014.

744

745 Berrington, A. H., Sakaeda, N., Dias, J., and Kiladis, G. N.: Relationships Between the Eastward Propagation of the Madden-
 746 Julian Oscillation and Its Circulation Structure, *JGR Atmospheres*, 127, e2021JD035806,
 747 <https://doi.org/10.1029/2021JD035806>, 2022.

748

749 Bushell, A. C., Anstey, J. A., Butchart, N., Kawatani, Y., Osprey, S. M., Richter, J. H., Serva, F., Braesicke, P., Cagnazzo, C.,
 750 Chen, C.-C., Chun, H.-Y., Garcia, R. R., Gray, L. J., Hamilton, K., Kerzenmacher, T., Kim, Y.-H., Lott, F., McLandress, C.,
 751 Naoe, H., Scinocca, J., Smith, A. K., Stockdale, T. N., Versick, S., Watanabe, S., Yoshida, K., and Yukimoto, S.: Evaluation
 752 of the Quasi-Biennial Oscillation in global climate models for the SPARC QBO-initiative, *Quart J Royal Meteor Soc*, 148,
 753 1459–1489, <https://doi.org/10.1002/qj.3765>, 2022.

754

755 Butchart, N., Anstey, J. A., Hamilton, K., Osprey, S., McLandress, C., Bushell, A. C., Kawatani, Y., Kim, Y.-H., Lott, F.,
 756 Scinocca, J., Stockdale, T. N., Andrews, M., Bellprat, O., Braesicke, P., Cagnazzo, C., Chen, C.-C., Chun, H.-Y., Dobrynin,
 757 M., Garcia, R. R., Garcia-Serrano, J., Gray, L. J., Holt, L., Kerzenmacher, T., Naoe, H., Pohlmann, H., Richter, J. H., Scaife,
 758 A. A., Schenzinger, V., Serva, F., Versick, S., Watanabe, S., Yoshida, K., and Yukimoto, S.: Overview of experiment design
 759 and comparison of models participating in phase 1 of the SPARC Quasi-Biennial Oscillation initiative (QBOi), *Geosci. Model*
 760 *Dev.*, 11, 1009–1032, <https://doi.org/10.5194/gmd-11-1009-2018>, 2018.

761

762 Chen, D., Lian, T., Fu, C., Cane, M. A., Tang, Y., Murtugudde, R., Song, X., Wu, Q., and Zhou, L.: Strong influence of
 763 westerly wind bursts on El Niño diversity, *Nature Geosci*, 8, 339–345, <https://doi.org/10.1038/ngeo2399>, 2015.

764

765 Chikira, M. and Sugiyama, M.: A Cumulus Parameterization with State-Dependent Entrainment Rate. Part I: Description and
 766 Sensitivity to Temperature and Humidity Profiles, *Journal of the Atmospheric Sciences*, 67, 2171–2193,
 767 <https://doi.org/10.1175/2010JAS3316.1>, 2010.

768

769 Das, U. and Pan, C. J.: Equatorial atmospheric Kelvin waves during El Niño episodes and their effect on stratospheric QBO,
770 Science of The Total Environment, 544, 908–918, <https://doi.org/10.1016/j.scitotenv.2015.12.009>, 2016.
771

772 Dasgupta, P., Roxy, M. K., Chattopadhyay, R., Naidu, C. V., and Metya, A.: Interannual variability of the frequency of MJO
773 phases and its association with two types of ENSO, Sci Rep, 11, 11541, <https://doi.org/10.1038/s41598-021-91060-2>, 2021.
774

775 Densmore, C. R., Sanabia, E. R., and Barrett, B. S.: QBO Influence on MJO Amplitude over the Maritime Continent: Physical
776 Mechanisms and Seasonality, Monthly Weather Review, 147, 389–406, <https://doi.org/10.1175/MWR-D-18-0158.1>, 2019.
777

778 Emanuel, K. A.: A Scheme for Representing Cumulus Convection in Large-Scale Models, J. Atmos. Sci., 48, 2313–2329,
779 [https://doi.org/10.1175/1520-0469\(1991\)048<2313:ASFRCC>2.0.CO;2](https://doi.org/10.1175/1520-0469(1991)048<2313:ASFRCC>2.0.CO;2), 1991.
780

781 Emori, S., Nozawa, T., Numaguti, A., and Uno, I.: Importance of Cumulus Parameterization for Precipitation Simulation over
782 East Asia in June., Journal of the Meteorological Society of Japan, 79, 939–947, <https://doi.org/10.2151/jmsj.79.939>, 2001.
783

784 Fernandes, L. G. and Grimm, A. M.: ENSO Modulation of Global MJO and Its Impacts on South America, Journal of Climate,
785 36, 7715–7738, <https://doi.org/10.1175/JCLI-D-22-0781.1>, 2023.
786

787 Gehne, M., Hamill, T. M., Kiladis, G. N., and Trenberth, K. E.: Comparison of Global Precipitation Estimates across a Range
788 of Temporal and Spatial Scales. Journal of Climate, 29(21), 7773–7795. <https://doi.org/10.1175/JCLI-D-15-0618.1>, 2016.
789

790 Hendon, H. H. and Abhik, S.: Differences in Vertical Structure of the Madden-Julian Oscillation Associated With the Quasi-
791 Biennial Oscillation, Geophysical Research Letters, 45, 4419–4428, <https://doi.org/10.1029/2018GL077207>, 2018.
792

793 Ham, S. and Hong, S.-Y.: Sensitivity of simulated intraseasonal oscillation to four convective parameterization schemes in a
794 coupled climate model, Asia-Pacific J Atmos Sci, 49, 483–496, <https://doi.org/10.1007/s13143-013-0043-9>, 2013.
795

796 Hansen, F., Matthes, K., and Gray, L. J.: Sensitivity of stratospheric dynamics and chemistry to QBO nudging width in the
797 chemistry–climate model WACCM, JGR Atmospheres, 118, <https://doi.org/10.1002/jgrd.50812>, 2013.
798

799 Hendon, H. H. and Salby, M. L.: The Life Cycle of the Madden–Julian Oscillation, J. Atmos. Sci., 51, 2225–2237,
800 [https://doi.org/10.1175/1520-0469\(1994\)051<2225:TLCOTM>2.0.CO;2](https://doi.org/10.1175/1520-0469(1994)051<2225:TLCOTM>2.0.CO;2), 1994.
801

802 Hendon, H. H., Zhang, C., and Glick, J. D.: Interannual Variation of the Madden–Julian Oscillation during Austral Summer,
803 J. Climate, 12, 2538–2550, [https://doi.org/10.1175/1520-0442\(1999\)012<2538:IVOTMJ>2.0.CO;2](https://doi.org/10.1175/1520-0442(1999)012<2538:IVOTMJ>2.0.CO;2), 1999.
804

805 Hendon, H. H., Wheeler, M. C., and Zhang, C.: Seasonal Dependence of the MJO–ENSO Relationship, Journal of Climate,
806 20, 531–543, <https://doi.org/10.1175/JCLI4003.1>, 2007.
807

808 Henley, B. J., Gergis, J., Karoly, D. J., Power, S., Kennedy, J., and Folland, C. K.: A Tripole Index for the Interdecadal Pacific
809 Oscillation, Clim Dyn, 45, 3077–3090, <https://doi.org/10.1007/s00382-015-2525-1>, 2015.
810

811 Hourdin, F., Grandpeix, J.-Y., Rio, C., Bony, S., Jam, A., Cheruy, F., Rochetin, N., Fairhead, L., Idelkadi, A., Musat, I.,
812 Dufresne, J.-L., Lahellec, A., Lefebvre, M.-P., and Roehrig, R.: LMDZ5B: the atmospheric component of the IPSL climate
813 model with revisited parameterizations for clouds and convection, Clim Dyn, 40, 2193–2222, <https://doi.org/10.1007/s00382-012-1343-y>, 2013.
814

815

816 Huang, K., Richter, J. H., and Pegion, K. V.: Captured QBO-MJO Connection in a Subseasonal Prediction System,
817 Geophysical Research Letters, 50, e2022GL102648, <https://doi.org/10.1029/2022GL102648>, 2023.
818

819 Huffman, G.J., R.F. Adler, M. Morrissey, D.T. Bolvin, S. Curtis, R. Joyce, B McGavock, J. Susskind: Global Precipitation at
820 One-Degree Daily Resolution from Multi-Satellite Observations. *J. Hydrometeor.*, 2(1), 36-50, doi.org/10.1175/1525-
821 7541(2001)002<0036:GPAODD>2.0.CO;2, 2001

822

823 Jiang, X., Waliser, D. E., Xavier, P. K., Petch, J., Klingaman, N. P., Woolnough, S. J., Guan, B., Bellon, G., Crueger, T.,
824 DeMott, C., Hannay, C., Lin, H., Hu, W., Kim, D., Lappen, C., Lu, M., Ma, H., Miyakawa, T., Ridout, J. A., Schubert, S. D.,
825 Scinocca, J., Seo, K., Shindo, E., Song, X., Stan, C., Tseng, W., Wang, W., Wu, T., Wu, X., Wyser, K., Zhang, G. J., and Zhu,
826 H.: Vertical structure and physical processes of the Madden-Julian oscillation: Exploring key model physics in climate
827 simulations, *JGR Atmospheres*, 120, 4718–4748, <https://doi.org/10.1002/2014JD022375>, 2015.

828

829 Jiang, X., Maloney, E., and Su, H.: Large-scale controls of propagation of the Madden-Julian Oscillation, *npj Clim Atmos Sci*,
830 3, 29, <https://doi.org/10.1038/s41612-020-00134-x>, 2020.

831

832 Jin, D., D. Kim, S.-W. Son, and L. Oreopoulos, 2023: QBO deepens MJO convection, *Nature Communications*, 14, 4088,
833 <https://doi.org/10.1038/s41467-023-39465-7>

834

835 Kang, I.-S., Liu, F., Ahn, M.-S., Yang, Y.-M., and Wang, B.: The Role of SST Structure in Convectively Coupled Kelvin–
836 Rossby Waves and Its Implications for MJO Formation, *Journal of Climate*, 26, 5915–5930, [https://doi.org/10.1175/JCLI-D-
837 12-00303.1](https://doi.org/10.1175/JCLI-D-12-00303.1), 2013.

838

839 Kawatani, Y., Hamilton, K., Sato, K., Dunkerton, T. J., Watanabe, S., and Kikuchi, K.: ENSO Modulation of the QBO: Results
840 from MIROC Models with and without Nonorographic Gravity Wave Parameterization, *Journal of the Atmospheric Sciences*,
841 76, 3893–3917, <https://doi.org/10.1175/JAS-D-19-0163.1>, 2019.

842

843 Kawatani, Y., Hamilton, K., Watanabe, S., M., Taguchi, Serva, F., Anstey, J. A., Richter, J. H., Butchart, N., Orbe, C., Osprey,
844 S. M., Naoe, H., Elsbury, D., Chen, C.-C., García-Serrano, J., Glanville, A., Kerzenmacher, T., Lott, F., Palmeiro, F. M., Park,
845 M., Versick, S., and Yoshida, K.: QBOi El Nino Southern Oscillation experiments Part I: Overview of experiment design and
846 ENSO modulation of the QBO, *Weather and Climate Dynamics* (in press), <https://doi.org/10.5194/egusphere-2024-3270>,
847 2025.

848

849 Kelley, M., Schmidt, G. A., Nazarenko, L. S., Bauer, S. E., Ruedy, R., Russell, G. L., Ackerman, A. S., Aleinov, I., Bauer, M.,
850 Bleck, R., Canuto, V., Cesana, G., Cheng, Y., Clune, T. L., Cook, B. I., Cruz, C. A., Del Genio, A. D., Elsaesser, G. S.,
851 Faluvegi, G., Kiang, N. Y., Kim, D., Lacis, A. A., Leboissetier, A., LeGrande, A. N., Lo, K. K., Marshall, J., Matthews, E. E.,
852 McDermid, S., Mezuman, K., Miller, R. L., Murray, L. T., Oinas, V., Orbe, C., García-Pando, C. P., Perlwitz, J. P., Puma, M.
853 J., Rind, D., Romanou, A., Shindell, D. T., Sun, S., Tausnev, N., Tsigaridis, K., Tselioudis, G., Weng, E., Wu, J., and Yao,
854 M.: GISS-E2.1: Configurations and Climatology, *J Adv Model Earth Syst*, 12, e2019MS002025,
855 <https://doi.org/10.1029/2019MS002025>, 2020.

856

857 Kessler, W. S.: EOF Representations of the Madden–Julian Oscillation and Its Connection with ENSO, *J. Climate*, 14, 3055–
858 3061, [https://doi.org/10.1175/1520-0442\(2001\)014<3055:EROTMJ>2.0.CO;2](https://doi.org/10.1175/1520-0442(2001)014<3055:EROTMJ>2.0.CO;2), 2001.

859

860 Kiladis, G. N., Wheeler, M. C., Haertel, P. T., Straub, K. H., and Roundy, P. E.: Convectively coupled equatorial waves,
861 *Reviews of Geophysics*, 47, 2008RG000266, <https://doi.org/10.1029/2008RG000266>, 2009.

862

863 Kim, D., Xavier, P., Maloney, E., Wheeler, M., Waliser, D., Sperber, K., Hendon, H., Zhang, C., Neale, R., Hwang, Y.-T., and
864 Liu, H.: Process-Oriented MJO Simulation Diagnostic: Moisture Sensitivity of Simulated Convection, *Journal of Climate*, 27,
865 5379–5395, <https://doi.org/10.1175/JCLI-D-13-00497.1>, 2014.

866

867 Kim, H., Caron, J. M., Richter, J. H., and Simpson, I. R.: The Lack of QBO-MJO Connection in CMIP6 Models, *Geophysical*
868 *Research Letters*, 47, e2020GL087295, <https://doi.org/10.1029/2020GL087295>, 2020.

869

870 Kim, J., K. M. Grise, and S.-W. Son, 2013: Thermal characteristics of the cold-point tropopause region in CMIP5 models,
871 Journal of Geophysical Research - Atmospheres, 118, 8827-8841.
872

873 Klotzbach, P., Abhik, S., Hendon, H. H., Bell, M., Lucas, C., G. Marshall, A., and Oliver, E. C. J.: On the emerging relationship
874 between the stratospheric Quasi-Biennial oscillation and the Madden-Julian oscillation, Sci Rep, 9, 2981,
875 <https://doi.org/10.1038/s41598-019-40034-6>, 2019.
876

877 Kumar, V., Yoden, S., and Hitchman, M. H.: QBO and ENSO Effects on the Mean Meridional Circulation, Polar Vortex,
878 Subtropical Westerly Jets, and Wave Patterns During Boreal Winter, JGR Atmospheres, 127,
879 e2022JD036691, <https://doi.org/10.1029/2022JD036691>, 2022.
880

881 Lawrence, Z. D., Elsbury, D., Butler, A. H., Perlwitz, J., Albers, J. R., Ciasto, L. M., and Ray, E.: Evaluation of Processes
882 Related to Stratosphere-Troposphere Coupling in GEFsV12 Subseasonal Hindcasts, Monthly Weather Review, 151, 1735–
883 1755, <https://doi.org/10.1175/MWR-D-22-0283.1>, 2023.
884

885 Liebmann, B., and Smith, C. A.: Description of a Complete (Interpolated) Outgoing Longwave Radiation Dataset, Bulletin of
886 the American Meteorological Society 77, 6, 1274–78. <https://doi.org/10.1175/1520-0477-77.6.1274>, 1996.
887

888 Lim, Y. and Son, S.: QBO-MJO Connection in CMIP5 Models, JGR Atmospheres, 125, e2019JD032157,
889 <https://doi.org/10.1029/2019JD032157>, 2020.
890

891 Lin, H.: The Madden-Julian Oscillation, Atmosphere-Ocean, 60, 338–359, <https://doi.org/10.1080/07055900.2022.2072267>,
892 2022.
893

894 Madden, R. A. and Julian, P. R.: Observations of the 40–50-Day Tropical Oscillation—A Review, Mon. Wea. Rev., 122, 814–
895 837, [https://doi.org/10.1175/1520-0493\(1994\)122<0814:OOTDIO>2.0.CO;2](https://doi.org/10.1175/1520-0493(1994)122<0814:OOTDIO>2.0.CO;2), 1994.
896

897 Martin, Z., S.-W. Son, A. Butler, H. Hendon, H. Kim, A. Sobel, S. Yoden, and C. Zhang, 2021: The influence of the Quasi-
898 Biennial Oscillation on the Madden-Julian Oscillation, Nature Reviews Earth & Environment, <https://doi.org/10.1038/s43017-021-00173-9>.
899

900 Martin, Z. K., Simpson, I. R., Lin, P., Orbe, C., Tang, Q., Caron, J. M., Chen, C., Kim, H., Leung, L. R., Richter, J. H., and
901 Xie, S.: The Lack of a QBO-MJO Connection in Climate Models With a Nudged Stratosphere, JGR Atmospheres, 128,
902 e2023JD038722, <https://doi.org/10.1029/2023JD038722>, 2023.
903

904 Matsuno, T.: Quasi-Geostrophic Motions in the Equatorial Area, Journal of the Meteorological Society of Japan, 44, 25–43,
905 https://doi.org/10.2151/jmsj1965.44.1_25, 1966.
906

907 Miura, H., Maeda, T., and Kimoto, M.: A Comparison of the Madden-Julian Oscillation Simulated by Different Versions of
908 the MIROC Climate Model, SOLA, 8, 165–169, <https://doi.org/10.2151/sola.2012-040>, 2012.
909

910 Nakamura, Y. and Takayabu, Y. N.: Convective Couplings with Equatorial Rossby Waves and Equatorial Kelvin Waves. Part
911 I: Coupled Wave Structures, Journal of the Atmospheric Sciences, 79, 247–262, <https://doi.org/10.1175/JAS-D-21-0080.1>,
912 2022.
913

914 Naoe, H., Garcia-Franco, J. L., Park, C.-H., Rodrigo, M., Palmeiro, F. M., Serva, F., Taguchi, M., Yoshida, K., Anstey, J. A.,
915 Garcia-Serrano, J., Son, S.-W., Kawatani, Y., Butchart, N., Hamilton, K., Chen, C.-C., Glanville, A., Kerzenmacher, T., Lott,
916 F., Orbe, C., Osprey, S., Park, M., Richter, J. H., Versick, S., and Watanabe, S.: QBOi El Niño Southern Oscillation
917 experiments: Teleconnections of the QBO, EGUsphere [preprint], <https://doi.org/10.5194/egusphere-2025-1148>, 2025.
918

919 Newman, M., Sardeshmukh, P. D., and Penland, C.: How Important Is Air–Sea Coupling in ENSO and MJO Evolution?,
920 Journal of Climate, 22, 2958–2977, <https://doi.org/10.1175/2008JCLI2659.1>, 2009.
921

922 Nordeng, T.-E.: Extended versions of the convective parametrization scheme at ECMWF and their impact on the mean and
923 transient activity of the model in the tropics, <https://doi.org/10.21957/E34XWHY5W>, 1994.

924

925 Orbe, C., Van Roekel, L., Adames, Á. F., Dezfuli, A., Fasullo, J., Gleckler, P. J., Lee, J., Li, W., Nazarenko, L., Schmidt, G.
926 A., Sperber, K. R., & Zhao, M.: Representation of Modes of Variability in Six U.S. Climate Models, *Journal of Climate*,
927 33(17), 7591–7617. <https://doi.org/10.1175/JCLI-D-19-0956.1>, 2020.

928

929 Pahlavan, H. A., Wallace, J. M., Fu, Q., and Kiladis, G. N.: Revisiting the Quasi-Biennial Oscillation as Seen in ERA5. Part
930 II: Evaluation of Waves and Wave Forcing, *Journal of the Atmospheric Sciences*, 78, 693–707, [https://doi.org/10.1175/JAS-](https://doi.org/10.1175/JAS-D-20-0249.1)
931 [D-20-0249.1](https://doi.org/10.1175/JAS-D-20-0249.1), 2021.

932

933 Pan, D. and Randall, D. D. A.: A cumulus parameterization with a prognostic closure, *Quart J Royal Meteorol Soc*, 124, 949–
934 981, <https://doi.org/10.1002/qj.49712454714>, 1998.

935

936 Pang, B., Chen, Z., Wen, Z., and Lu, R.: Impacts of two types of El Niño on the MJO during boreal winter, *Adv. Atmos. Sci.*,
937 33, 979–986, <https://doi.org/10.1007/s00376-016-5272-2>, 2016.

938

939 Pascoe, C. L., Gray, L. J., Crooks, S. A., Jukes, M. N., and Baldwin, M. P.: The quasi-biennial oscillation: Analysis using
940 ERA-40 data, *J. Geophys. Res.*, 110, 2004JD004941, <https://doi.org/10.1029/2004JD004941>, 2005.

941

942 Philander, S. G.: *El Niño, La Niña, and the southern oscillation*, Academic Press, San Diego, 293 pp., 1990.

943

944 Pohl, B. and Matthews, A. J.: Observed Changes in the Lifetime and Amplitude of the Madden–Julian Oscillation Associated
945 with Interannual ENSO Sea Surface Temperature Anomalies, *Journal of Climate*, 20, 2659–2674,
946 <https://doi.org/10.1175/JCLI4230.1>, 2007.

947

948 Puy, M., Vialard, J., Lengaigne, M., and Guilyardi, E.: Modulation of equatorial Pacific westerly/easterly wind events by the
949 Madden–Julian oscillation and convectively-coupled Rossby waves, *Clim Dyn*, 46, 2155–2178,
950 <https://doi.org/10.1007/s00382-015-2695-x>, 2016.

951

952 Randall, D. A., Tziperman, E., Branson, M. D., Richter, J. H., and Kang, W.: The QBO–MJO Connection: A Possible Role
953 for the SST and ENSO, *Journal of Climate*, 36, 6515–6531, <https://doi.org/10.1175/JCLI-D-23-0031.1>, 2023.

954

955 Richter, J. H., Anstey, J. A., Butchart, N., Kawatani, Y., Meehl, G. A., Osprey, S., and Simpson, I. R.: Progress in Simulating
956 the Quasi-Biennial Oscillation in CMIP Models, *JGR Atmospheres*, 125, e2019JD032362,
957 <https://doi.org/10.1029/2019JD032362>, 2020.

958

959 Rind, D., Jonas, J., Balachandran, N. K., Schmidt, G. A., and Lean, J.: The QBO in two GISS global climate models: 1.
960 Generation of the QBO, *JGR Atmospheres*, 119, 8798–8824, <https://doi.org/10.1002/2014JD021678>, 2014.

961

962 Rind, D., Orbe, C., Jonas, J., Nazarenko, L., Zhou, T., Kelley, M., Lacis, A., Shindell, D., Faluvegi, G., Romanou, A., Russell,
963 G., Tausnev, N., Bauer, M., and Schmidt, G.: GISS Model E2.2: A Climate Model Optimized for the Middle Atmosphere—
964 Model Structure, Climatology, Variability, and Climate Sensitivity, *JGR Atmospheres*, 125, e2019JD032204,
965 <https://doi.org/10.1029/2019JD032204>, 2020.

966

967 Roundy, P. E.: The Spectrum of Convectively Coupled Kelvin Waves and the Madden–Julian Oscillation in Regions of Low-
968 Level Easterly and Westerly Background Flow, *Journal of the Atmospheric Sciences*, 69, 2107–2111,
969 <https://doi.org/10.1175/JAS-D-12-060.1>, 2012.

970

971 Sakaeda, N., Dias, J., and Kiladis, G. N.: The Unique Characteristics and Potential Mechanisms of the MJO–QBO Relationship,
972 *JGR Atmospheres*, 125, e2020JD033196, <https://doi.org/10.1029/2020JD033196>, 2020.

973

974 Schenzinger, V., Osprey, S., Gray, L., and Butchart, N.: Defining metrics of the Quasi-Biennial Oscillation in global climate
975 models, *Geosci. Model Dev.*, 10, 2157–2168, <https://doi.org/10.5194/gmd-10-2157-2017>, 2017.
976

977 Schreck, C. J.: Global Survey of the MJO and Extreme Precipitation, *Geophysical Research Letters*, 48,
978 e2021GL094691, <https://doi.org/10.1029/2021GL094691>, 2021.
979

980 Serva, F., Anstey, J. A., Bushell, A. C., Butchart, N., Cagnazzo, C., Gray, L. J., Kawatani, Y., Osprey, S. M., Richter, J. H.,
981 and Simpson, I. R.: The impact of the QBO on the region of the tropical tropopause in QBOi models: Present-day simulations,
982 *Quart J Royal Meteorol Soc*, 148, 1945–1964, <https://doi.org/10.1002/qj.4287>, 2022.
983

984 Serva, F., Christiansen, B., Davini, P., Von Hardenberg, J., Van Den Oord, G., Reerink, T. J., Wyser, K., and Yang, S.: Changes
985 in Stratospheric Dynamics Simulated by the EC-Earth Model From CMIP5 to CMIP6, *J Adv Model Earth Syst*, 16,
986 e2023MS003756, <https://doi.org/10.1029/2023MS003756>, 2024.
987

988 Slingo, J. M., Rowell, D. P., Sperber, K. R., and Nortley, F.: On the predictability of the interannual behaviour of the Madden-
989 Julian oscillation and its relationship with el Niño, *Quart J Royal Meteorol Soc*, 125, 583–609,
990 <https://doi.org/10.1002/qj.49712555411>, 1999.
991

992 Son, S.-W., Lim, Y., Yoo, C., Hendon, H. H., and Kim, J.: Stratospheric Control of the Madden–Julian Oscillation, *Journal of*
993 *Climate*, 30, 1909–1922, <https://doi.org/10.1175/JCLI-D-16-0620.1>, 2017.
994

995 Straub, K. H. and Kiladis, G. N.: Observations of a Convectively Coupled Kelvin Wave in the Eastern Pacific ITCZ, *J. Atmos.*
996 *Sci.*, 59, 30–53, [https://doi.org/10.1175/1520-0469\(2002\)059<0030:OOACCK>2.0.CO;2](https://doi.org/10.1175/1520-0469(2002)059<0030:OOACCK>2.0.CO;2), 2002.
997

998 Suematsu, T. and Miura, H.: Zonal SST Difference as a Potential Environmental Factor Supporting the Longevity of the
999 Madden–Julian Oscillation, *Journal of Climate*, 31, 7549–7564, <https://doi.org/10.1175/JCLI-D-17-0822.1>, 2018.
1000

1001 Suematsu, T. and Miura, H.: Changes in the Eastward Movement Speed of the Madden–Julian Oscillation with Fluctuation in
1002 the Walker Circulation, *Journal of Climate*, 35, 211–225, <https://doi.org/10.1175/JCLI-D-21-0269.1>, 2022.
1003

1004 Sun, L., Wang, H., and Liu, F.: Combined effect of the QBO and ENSO on the MJO, *Atmospheric and Oceanic Science*
1005 *Letters*, 12, 170–176, <https://doi.org/10.1080/16742834.2019.1588064>, 2019.
1006

1007 Tam, C.-Y. and Lau, N.-C.: Modulation of the Madden-Julian Oscillation by ENSO: Inferences from Observations and GCM
1008 Simulations, *Journal of the Meteorological Society of Japan*, 83, 727–743, <https://doi.org/10.2151/jmsj.83.727>, 2005.
1009

1010 Tegtmeier, S., Anstey, J., Davis, S., Ivanciu, I., Jia, Y., McPhee, D., and Pilch Kedzierski, R.: Zonal Asymmetry of the QBO
1011 Temperature Signal in the Tropical Tropopause Region, *Geophysical Research Letters*, 47, e2020GL089533,
1012 <https://doi.org/10.1029/2020GL089533>, 2020.
1013

1014 Tiedtke, M.: A Comprehensive Mass Flux Scheme for Cumulus Parameterization in Large-Scale Models, *Mon. Wea. Rev.*,
1015 117, 1779–1800, [https://doi.org/10.1175/1520-0493\(1989\)117<1779:ACMFSF>2.0.CO;2](https://doi.org/10.1175/1520-0493(1989)117<1779:ACMFSF>2.0.CO;2), 1989.
1016

1017 Vitart, F.: Madden—Julian Oscillation prediction and teleconnections in the S2S database, *Quart J Royal Meteorol Soc*, 143,
1018 2210–2220, <https://doi.org/10.1002/qj.3079>, 2017.
1019

1020 Waliser, D., Sperber, K., Hendon, H., Kim, D., Maloney, E., Wheeler, M., Weickmann, K., Zhang, C., Donner, L., Gottschalck,
1021 J. and Higgins, W. MJO simulation diagnostics. *J. Climate*, 22, 3006–3030, <https://doi.org/10.1175/2008JCLI2731.1>, 2009
1022

1023 Wang, B., Chen, G., and Liu, F.: Diversity of the Madden-Julian Oscillation, *Sci. Adv.*, 5, eaax0220,
1024 <https://doi.org/10.1126/sciadv.aax0220>, 2019.
1025

1026 Wang, T. and Li, T.: Diversity of MJO Initiation Regions and Processes, *Journal of Climate*, 35, 3121–3140,
1027 <https://doi.org/10.1175/JCLI-D-21-0816.1>, 2022.
1028

1029 Wang, Y.-C., Tseng, W.-L., and Hsu, H.-H.: Role of convection–circulation coupling in the propagation mechanism of the
1030 Madden–Julian Oscillation over the Maritime Continent in a climate model, *Clim Dyn*, 58, 2469–2484,
1031 <https://doi.org/10.1007/s00382-021-06013-2>, 2022.
1032

1033 Wei, Y. and Ren, H.-L.: Modulation of ENSO on Fast and Slow MJO Modes during Boreal Winter, *Journal of Climate*, 32,
1034 7483–7506, <https://doi.org/10.1175/JCLI-D-19-0013.1>, 2019.
1035

1036 Wheeler, M. C. and Hendon, H. H.: An All-Season Real-Time Multivariate MJO Index: Development of an Index for
1037 Monitoring and Prediction, *Mon. Wea. Rev.*, 132, 1917–1932, [https://doi.org/10.1175/1520-0493\(2004\)132<1917:AARMMI>2.0.CO;2](https://doi.org/10.1175/1520-0493(2004)132<1917:AARMMI>2.0.CO;2), 2004.
1038

1039

1040 Yadav, P. and Straus, D. M.: Circulation Response to Fast and Slow MJO Episodes, *Monthly Weather Review*, 145, 1577–
1041 1596, <https://doi.org/10.1175/MWR-D-16-0352.1>, 2017.
1042

1043 Yadav, P., Garfinkel, C. I., and Domeisen, D. I. V.: The Role of the Stratosphere in Teleconnections Arising From Fast and
1044 Slow MJO Episodes, *Geophysical Research Letters*, 51, e2023GL104826, <https://doi.org/10.1029/2023GL104826>, 2024.
1045

1046 Yoo, C., and S.-W. Son, 2016: Modulation of the boreal wintertime Madden-Julian Oscillation by the stratospheric Quasi-
1047 Biennial Oscillation, *Geophysical Research Letters*, 43, 1392–1398.
1048

1049 Yukimoto, S., Kawai, H., Koshiro, T., Oshima, N., Yoshida, K., Urakawa, S., Tsujino, H., Deushi, M., Tanaka, T., Hosaka,
1050 M., Yabu, S., Yoshimura, H., Shindo, E., Mizuta, R., Obata, A., Adachi, Y., and Ishii, M.: The Meteorological Research
1051 Institute Earth System Model Version 2.0, MRI-ESM2.0: Description and Basic Evaluation of the Physical Component,
1052 *Journal of the Meteorological Society of Japan*, 97, 931–965, <https://doi.org/10.2151/jmsj.2019-051>, 2019.
1053

1054 Yuni, A. R. E., Lubis, S. W., and Setiawan, S.: Vertical structure of Convectively Coupled Equatorial Waves (CCEWs) during
1055 Boreal Summer and Winter, *IOP Conf. Ser.: Earth Environ. Sci.*, 284, 012010, <https://doi.org/10.1088/1755-1315/284/1/012010>, 2019.
1056

1057

1058 Zhang, C. and Gottschalck, J.: SST Anomalies of ENSO and the Madden–Julian Oscillation in the Equatorial Pacific*, *J.*
1059 *Climate*, 15, 2429–2445, [https://doi.org/10.1175/1520-0442\(2002\)015<2429:SAOEAT>2.0.CO;2](https://doi.org/10.1175/1520-0442(2002)015<2429:SAOEAT>2.0.CO;2), 2002.
1060

1061 Zhang, G. J. and McFarlane, N. A.: Sensitivity of climate simulations to the parameterization of cumulus convection in the
1062 Canadian climate centre general circulation model, *Atmosphere-Ocean*, 33, 407–446,
1063 <https://doi.org/10.1080/07055900.1995.9649539>, 1995.
1064

1065 Zhu, J., Kumar, A., and Wang, W.: Dependence of MJO Predictability on Convective Parameterizations, *Journal of Climate*,
1066 33, 4739–4750, <https://doi.org/10.1175/JCLI-D-18-0552.1>, 2020.
1067
1068